ISTANBUL TECHNICAL UNIVERSITY ★ GRADUATE SCHOOL OF SCIENCE

CERN LARGE HADRON COLLIDER
COMPACT MUON SOLENOID
HADRONIC CALORIMETER UPGRADE WORKS

M.Sc. THESIS

Serhat ATAY

Department of Physics Engineering

Physics Engineering Programme

JUNE 2016

ISTANBUL TECHNICAL UNIVERSITY ★ GRADUATE SCHOOL OF SCIENCE

CERN LARGE HADRON COLLIDER
COMPACT MUON SOLENOID
HADRONIC CALORIMETER UPGRADE WORKS

M.Sc. THESIS

Serhat ATAY
(509131111)

Department of Physics Engineering

Physics Engineering Programme

Thesis Advisor: Assoc. Prof. Dr. Kerem Cankoçak

JUNE 2016

İSTANBUL TEKNİK ÜNİVERSİTESİ ★ FEN BİLİMLERİ ENSTİTÜSÜ

CERN BÜYÜK HADRON ÇARPIŞTIRICISI KOMPAKT MUON SOLENOİDİ HADRON KALORİMETRESİ YÜKSELTME İŞLERİ

YÜKSEK LİSANS TEZİ

Serhat ATAY
(509131111)

Fizik Mühendisliği Anabilim Dalı

Fizik Mühendisliği Programı

Tez Danışmanı: Assoc. Prof. Dr. Kerem Cankoçak

HAZİRAN 2016

Serhat ATAY, a M.Sc. student of ITU Graduate School of ScienceEngineering and Technology 509131111 successfully defended the thesis entitled “CERN LARGE HADRON COLLIDER COMPACT MUON SOLENOID HADRONIC CALORIMETER UPGRADE WORKS”, which he prepared after fulfilling the requirements specified in the associated legislations, before the jury whose signatures are below.

Thesis Advisor :	**Assoc. Prof. Dr. Kerem Cankoçak** Istanbul Technical University	....
Jury Members :	**Prof. Dr. Cenap Şahabettin Özben** Istanbul Technical University	....
	Prof. Dr. Erhan Gülmez Boğaziçi University	....
		....

Date of Submission : **2 May 2016**
Date of Defense : **6 June 2016**

To my family and beloved girlfriend,

FOREWORD

I would like to thank to my advisor Assoc. Prof. Dr. Kerem Cankoçak for his unconditional support for my thesis and for giving me a chance to work at The European Organization for Nuclear Research (CERN).

I would like to thank to Prof. Dr. Yaşar Önel from University of Iowa for helping me to work with CMS-Iowa group. Also special thanks to Alexi Mestvirishvili for helping and teaching me about analysis of all my work. Further thank to Viktor Khristenko about precious help for my analysis.

I would like to thank to my father Mustafa Atay, my mother Aynur Atay and my brother İbrahim Atay for supporting all my decisions, instead of judging, related to my career and my life.

I would like thank you my beloved girlfriend Tuğçe Algül for helping and motivating me when I was saturated and making my life meaningful.

I would like to thank you my co-worker Zafer Devrim with helpful discussions.

I would like to thank you Turkish Atomic Energy Authority (TAEK) for financial support during my thesis study in frame of 2014 TAEK (CERN) A5.H6.F2-09 Detector upgrade for phase II and new particles search beyond the Standart Model in the LHC-CMS experiment project.

June 2016

Serhat ATAY
Physicist and Mathematician

TABLE OF CONTENTS

Page

ABBREVIATIONS

ADC	: analog to digital converter
ALICE	: A Large Ion Collider Experiment
ATLAS	: A Toroidal Large Hadron Collider ApparatuS
BE	: back-end
BEBC	: The Big European Bubble Chamber
BESSY	: Berlin Electron Storage Ring Society for Synchrotron Radiation
BDV	: breakdown voltage
BNL	: Brookhaven National Laboratory
Caltech	: California Institute of Technology
CASTOR	: Centauro And Strange Object Research
CDF	: The Collider Detector at Fermilab
CERN	: The European Organization for Nuclear Research
CMS	: Compact Muon Solenoid
CMSSW	: Compact Muon Solenoid software package
CondDB	: conditions database
DAQ	: data acquisition
DELPHI	: Detector with Lepton, Photon and Hadron Identification
DESY	: German Electron Synchrotron
D∅	: D∅ experiment at Fermilab
ECAL	: electromagnetic calorimeter
ELETTRA	: Elettra Sincrotrone Trieste
ESRF	: European Synchrotron Radiation Facility
FE	: front-end
FNAL	: Fermi National Accelerator Laboratory
GPIB	: General Purpose Interface Bus
HASYLAB	: Hamburg Synchrotron Laboratory
HB	: hadronic barrel
HCAL	: hadronic calorimeter
HE	: hadronic endcap
HF	: hadronic forward
HFM	: hadronic forward minus
HFP	: hadronic forward plus
HL-LHC	: High Luminosity Large Hadron Collider
HO	: hadronic outer
HPD	: hybrid photo diode
I-V	: current-voltage
KEK	: The High Energy Accelerator Research Organization
LEP	: The Large Electron-Positron Collider
LHC	: The Large Hadron Collider
LHCb	: Large Hadron Collider beauty
LINAC2	: Linear Accelerator 2
LS1	: long shutdown 1

LS2	: long shutdown 2
LS3	: long shutdown 3
MIP	: minimum ionizing particle
NbTi	: niobium-titanium alloy
ngCCM	: new generation clock control module
ngRBXManager	: new generation readout boxes manager
PMT	: photomultiplier tube
PS	: The Proton Synchrotron
PSB	: The Proton Synchrotron Booster
QE	: quantum efficiency
QIE	: charge integrated encoder
RBX	: readout boxes
RCMS	: the run control and monitor system
RCT	: regional calorimeter trigger
RF	: radio frequency
RM	: readout module
RMS	: root mean square
SiPM	: silicon photomultiplier
SLAC	: Stanford Linear Accelerator Center
SPS	: The Super Proton Synchrotron
TDC	: time to digital converter
TS	: time slice
UA1	: The Underground Area 1
UI	: University of Iowa
UMD	: University of Maryland
USA	: United States of America
USC	: underground service cavern
UV	: ultra violet
V-A	: vector - axial vector theory
WLS	: wave length shifter

LIST OF TABLES

Page

LIST OF FIGURES

Page

CERN LARGE HADRON COLLIDER
COMPACT MUON SOLENOID
HADRONIC CALORIMETER UPGRADE WORKS

SUMMARY

The Large Hadron Collider (LHC) and its detectors have become the most discussed scientific device around the world with its discoveries. Starting from 2000s, LHC project became real in March 2010, the first successful collision. Just in 2 years, LHC discovered Higgs boson on July 4, 2012.

LHC houses 4 big experiments, Compact Muon Solenoid (CMS), A Toroidal Large Hadron Collider ApparatuS (ATLAS), A Large Ion Collider Experiment (ALICE) and Large Hadron Collider beauty (LHCb). CMS is the heaviest and one of general purpose detector of LHC. CMS has hadronic calorimeter (HCAL) to measure and identify hadrons. HCAL consists of hadronic barrel (HB), hadronic outer (HO), hadronic endcap (HE) and hadronic forward (HF) calorimeters.

Material of these detectors will be damaged due to increasing integrated radiation for high luminosity of LHC. For that reason, material of subsystems needs to be replaced by stronger ones. For example, hadronic endcap scintillators will be highly damaged by luminosity of High Luminosity Large Hadron Collider (HL-LHC), new phase of LHC starting from 2023. For replacement, 4 different institutes have proposed new scintillators. Irradiation test of these scintillators were done with a dark box, silicon photomultiplier (SiPM) and a readout system in 2015. Measurements were taken in March, June, September and December 2015. In order to understand how much these scintillators will be damaged by radiation, installation box of scintillators were irradiated by installing few cm close to the beam pipe inside the CMS detector –to Centauro And Strange Object Research (CASTOR) table. After taking derivatives of measurement data under different conditions, breakdown voltage (BDV) of SiPMs were calculated in ROOT software package. Adding a specific voltage to BDV, currents were compared to observe radiation damage in scintillators.

Due to systematical and statistical errors in previous measurements setup new measurements will be taken via HCAL data acquisition (DAQ) system for reliable results. Work are still continue as of April 2016.

In long shutdown 1 (LS1) photomultiplier tubes (PMT) of HF calorimeters were replaced by new ones. To calibrate new PMTs, sourcing data were taken with Co-60 radioactive source, and analysis were done in CMSSW. Applying several corrections and conversions, calibration coefficients of individual PMTs were calculated. New source data were taken in 2016 and analysis of new data were scheduled later this year.

Alongside these tasks, there are several ongoing tasks such as HF radiation damage monitoring and online software development. HF-fiber radiation damage monitoring involves local radiation damage data in CMMSW and monitor radiation damage in time. Online software includes developing and upgrading new generation readout box

manager (ngRBXManager). This software will operate to take data from readout boxes via new generation clock control module (ngCCM).

CERN BÜYÜK HADRON ÇARPIŞTIRICISI KOMPAKT MUON SOLENOİDİ HADRON KALORİMETRESİ YÜKSELTME İŞLERİ

ÖZET

Günümüzden yaklaşık 13,8 milyar yıl önce Büyük Patlamayla başlayan parçacıkların serüveni günümüz fizikçilerinin en merak ettiği konulardan biridir. Büyük Patlamayla oluşan parçacık ve karşı-parçacıklar büyük oranda birbirleriyle etkileşime girerek yok olmuşlardır. Fakat eşit miktarda oluşması beklenen parçacık ve karşı-parçacıklar, parçacıklar lehine yaklaşık %5 oranında kendiliğinden bozulmuştur. Parçacıkların günümüze doğru devam eden serüvenine yaklaşık 160.000 yıl önce dahil olan homo sapiensler, parçacıklar evrenini keşfetmeye başlamışlardır. M.Ö. 4. yüzyılda Demokritos, maddenin parçalanamayan küçük parçacıklardan yani atomlardan oluştuğu fikrini ortaya atmıştır. Fakat atomun gözlenmesi 19. yüzyılın sonuna kadar mümkün olmamıştır. 1897'de J. J. Thomson'ın elektronu keşfiyle başlayan parçacık fiziği serüveni hızlı bir şekilde seyir almıştır. 1911'de Rutherford'un atom modeli ve bulut odasının keşfiyle birlikte yeni parçacıklar gözlenmeye ve gözlem teknikleri gelişmeye başlamıştır. Atmosferimize çarparak yeryüzüne ulaşan kozmik ışınlarda düşük kütleli parçacıklar gözlenmeye başlandı. 1950'lere gelindiğinde kozmik ışınların enerjisinin düşük olmasından dolayı yeni parçacıklar gözlenmemeye başlandı. Bilim topluluğu bu duruma hızlandırıcılar icat ederek çözüm buldu. Bu sayede parçacıklara elektrik alan altında enerji kazandırılıp hedefe çarptırılarak yüksek kütleli parçacıkların da gözlenmesi sağlandı.

1950'lerin sonunda Avrupa'da İkinci Dünya Savaşı sonrası sadece hayatlar değil, bilim de durma noktasına gelmişti. Bu sebeple 1952 yılında aralarında Werner Heisenberg gibi Nobel ödülü sahibi bilim insanlarının da bulunduğu bir konsey toplandı. Konseyin toplantıları sonucu 1954 yılında İsviçre'nin Cenevre kenti yakınlarında Avrupa Nükleer Araştırma Merkezi (CERN) kuruldu. CERN hızlandırıcı dünyasına Eş Zamanlı Siklotron (SC) ve Proton Eş Zamanlayıcısıyla (PS) birlikte hızlı bir giriş yaptı. SC, 1957 yılında pion parçacığının elektrona bozunumunu gözleyerek vektör - aksiyal vektör (V-A) kuramını doğruladı. Bu keşifle birlikte CERN yıllar içinde yeni hızlandırıcılar yapmaya devam etti. 1976 yılında Süper Proton Eş Zamanlayıcısı (SPS) tamamlandı. Bu eş zamanlayıcı, protonları 450 GeV enerjisine kadar hızlandırabilmektedir. 1983 yılında proton karşı-proton çarpıştırıcısı çalışmaya başladı ve UA1 deneyinde $W^{\pm}$ ve Z^0 bozonları keşfedildi. 1989 yılına gelindiğinde 27 kilometre uzunluğundaki Büyük Elektron-Pozitron Çarpıştırıcısı (LEP) hayata geçti. Elektron ve pozitronları çarpıştıran bu hızlandırıcı, 200 GeV enerjisine ulaşabiliyordu. 2000'li yılların başında, CERN'de dünya çapında ses getirecek olan yeni bir proje başladı. Büyük Elektron-Pozitron Çarpıştırıcısı, Büyük Hadron Çarpıştırıcısıyla (LHC) değiştirildi. 2010 yılında çarpışmalara başlanan LHC'de 4 büyük algıç bulunmaktadır. Bunlardan ikisi genel amaçlı algıçlar olmak üzere Toroidal Büyük Hadron Çarpıştırıcısı Aparatı (ATLAS) ve Kompakt Muon Solenoididir (CMS). Diğer

ikisi belirli amaçlar için tasarlanmış olan Büyük İyon Çarpıştırma (ALICE) ve Büyük Hadron Çarpıştırıcısı Alt Kuark (LHCb) deneyleridir.

CMS deneyi 2012 yılında ATLAS'la birlikte Higgs bozonunu keşfetmiştir. Fakat yerin 100 metre altındaki mağaralarda bulunan bu algıçlar oluşan yoğun radyasyondan dolayı etkilenmektedirler. Algıçların elektronik parçaları ve parçacık tespitini sağlayan mekanik parçaları radyasyondan zarar görmelerinden bağımsız olarak algıçlarda yükseltme işlemleri de gerekmektedir. Yeni parçacıklar keşfedildikçe, daha yüksek kütleli parçacıkların gözlenmesi için daha yüksek ışınlıklı ve daha yüksek enerjili çarpışmalar yapılması gerekmektedir.

CMS algıcının hadron kalorimetresi, hadronların enerjisini soğurarak ölçen bir alt algıçtır. Varil şeklinde olan hadronik varil (HB) ve varili iki taraftan kapatan hadronik kapak (HE) kalorimetreleri vardır. Solenoid magnetin hemen dışında varil seklinde bir hadronik dış kalorimetresi (HO) vardır. İleri bölgede yüksek enerjili jetleri ve kayıp enine enerjiyi ölçen ileri hadron kalorimetreleri (HF) vardır. HE kalorimetresinin parçacık etkileşiminde foton oluşturan sintilatörleri, yüksek ışınlıklı LHC (HL-LHC) denilen 2020'de başlayacak olan yeni LHC dönemindeki radyasyona karşı dayanıklı olacak şekilde tasarlanmamıştır. Bu sebeple 4 farklı enstitünün önerdiği sintilatörlerden biriyle değiştirilmesi gerekmektedir. Önerilen sintilatörler 2015 yılı içerisinde CMS üzerinde CASTOR boşluğunda demet hattının birkaç cm yakınında radyasyona maruz bırakılmıştır. Sintilatörler CASTOR boşluğuna yerleştirilmeden önce mart ayında ölçümleri alınmıştır. Daha sonra haziran, eylül ve aralıktaki teknik aralarda tekrar yüzeye çıkarılıp ölçümleri yapılmıştır. İlk yapılan ölçümü referans kabul ederek sonraki ölçümlerde sintilatörün radyasyondan ne kadar zarar gördüğü ölçülmeye çalışılmıştır.

Ölçümler ışığı izole etmek için siyah bir kutu içinde silikon foto çoğaltıcı kullanılarak yapılmıştır. Silikon foto çoğaltıcıların kazançları kutuplama gerilimine ve sıcaklığa bağlıdır. Sintilatörler beta kaynağı olan ve radyoaktivitesi bilinen Sr-90 elementine maruz bırakılmıştır. Foto çoğaltıcıdan okunan akım değeri radyasyon kaynağının sintilatörde oluşturabileceği foton sayısıyla ilişkilidir. Bu sebeple veriler kutuplama gerilimine karşılık foto çoğaltıcıdan okunan akımın yer aldığı akım-gerilim grafiğidir. Foto çoğaltıcıların çalışma gerilim aralığını tespit etmek için ROOT yazılım programı aracılığıyla bu grafiğin sayısal türevi alınarak ilgili akım değerine bölünmüştür. Yeni grafikte iki tane tepe oluşur. İlk tepe çöküm gerilimi (BDV), ikinci tepe Geiger modudur. Geiger modundan sonra kaçak akımla karanlık akım ayrıştırılamaz. Çalışma aralığı bu iki tepe arasındadır. Belirli bir ΔV gerilimi, her ölçüm için Gaussyen uydurmasıyla ayrı ayrı hesaplanmış olan çöküm geriliminin üzerine eklenmiştir. Bu sayede foto çoğaltıcının kazancını etkileyen sıcaklık ve kutuplama gerilimi etkileri ortadan kaldırılmış olur. Her bağımsız ölçüm için ayrı ayrı elde edilen $BDV + \Delta V$ gerilimlerine karşılık gelen akımlar kıyaslanarak radyasyon hasarı belirlenmeye çalışılmıştır.

Mart ayında yapılan tekrarlanabilirlik ölçümlerine göre deney düzeneği yaklaşık %5 civarında sistematik hataya sahiptir. Ayrıca ölçümler 50 mV aralıklarla alınmıştır ve çalışma gerilimi aralığında iki komşu gerilim değerine karşı gelen akımlar arasında %10 fark vardır. Çöküm geriliminin iki komşu gerilimin tam ortasına gelmesi durumunda (yani çöküm geriliminin iki komşu gerilimden 25 mV uzakta olması durumunda) %5 mertebesinde istatistiksel hata mevcuttur. Her ne kadar istatistiksel hata, kübik iç-kestirimle azaltılmışsa da sistematik hata hâlâ kabul edilemez seviyededir. Bunun yansıra ölçümler yapılırken fiber kablo yetersizliği yüzünden aynı fiber kablo çeşitli sintilatörlere yerleştirilmiştir. Bu durum, fiber kabloya zarar vererek ileteceği ışık miktarını etkilemiştir.

Bu koşullar altında deney sonuçları beklenildiği üzere çok sağlıklı olmamıştır. Ölçümler arasındaki oranların 0 ile 1 arasında olması ve zamanla azalması beklenirken, bazı oranlar 1'den büyük bazıları eksi, bazı oranlar da zaman içinde artmıştır. Mevcut deney düzeneğinin verimli sonuç vermemesinden dolayı radyasyona maruz bırakma ölçümleri hadron kalorimetresinin veri alma sistemi kullanılarak daha stabil bir şekilde algıç üzerinden alınacaktır. Bu sayede tüm çevresel etkiler en aza inecek ve çok daha verimli veri alma sisteminin yanı sıra yeni algoritmalar sayesinde sistematik ve istatistik hatalar en aza inecektir. Yeni deney sistemi için çalışmalar nisan 2016 itibariyle devam etmektedir.

Bunların yanı sıra uzun yükseltme 1 (LS1), döneminde ileri hadron kalorimetresinin foto çoğaltıcı tüpleri daha fazla foton üreten yeni foto çoğaltıcılarla değiştirilmiştir. Yeni foto çoğaltıcı tüpler birbirinin aynısı olsa bile çevresel faktörlerden dolayı her birinin kalibre edilmesi gerekmektedir. Bu sebeple 2014 yılı içerisinde HF'nin her iki sektörü için Co-60 kaynağıyla veri alınmıştır. Bu veriler her tüpe teker teker radyoaktif kaynak sokularak tüm fiber boyunca alınmıştır.

CMSSW yazılım paketi aracılığıyla kaynak, ilgili tüpteyken ve ilgili tüpten uzaktayken olmak üzere iki farklı analiz yapılmıştır. Kaynak, tüpteyken alınan veriye sinyal; kaynak, uzaktayken alınan veri ardalandır. Veriler analog-dijital dönüştürücü (ADC) aracılığıyla alınır. Veri, farklı ağırlıklara sahip olacak şekilde 32'ye bölünmüş olarak bir histograma kaydedilir. Her bir kutunun Coulomb cinsinden bir değeri vardır. Bu sinyaller hesaplanırken, her bir olay histogramının sol tarafında yer alan tepenin orta noktasına karşılık gelen yük ilgili sinyalden çıkarılmıştır. Bu tepe, kapasitörlerin oluşturduğu pedestal denen yüklerdir. Bu şekilde hem ardalan hem de sinyal hesaplanmıştır. Daha sonra ardalan sinyali, sinyalden çıkarılarak arkaplandaki gürültüden kurtulunmuştur.

Elde edilen yüklere geometrik düzeltme uygulanmıştır. HF kalorimetresinin hücre büyüklükleri birbirinden farklı olduğu için hücrelerde soğrulan enerji miktarları farklı olacaktır. Bu geometrik düzeltme katsayıları Geant4 benzetim programıyla belirlenmiştir. Her bir foto çoğaltıcı tüp için okunan değer foto çoğaltıcıların üreticisi Hamamatsu firmasının kitapçığında yazan 2,6 ile çarpılarak femto-Coulomb (fC) cinsinden yükler olarak hesaplanmıştır. Daha sonra son düzeltme, yük (fC) cinsinden enerjiye (GeV) olan dönüşümdür. Bu dönüşüm için hadronik ve elektromanyetik tüplerde farklı enerji katsayıları kullanılmıştır. Sonuç olarak yeni foto çoğaltıcıların kalibrasyon katsayıları hesaplanmıştır. Bu katsayılarla foto çoğaltıcılarda indüklenen elektrik yükü, enerjiye dönüştütülebilmektedir. Bu sayede foto çoğaltıcı tarafından tespit edilen parçacığın enerjisi ölçülebilmektedir. Katsayılar yeni analizlerde kullanılması için veri tabanına kaydedilmiştir.

Aynı veriler 2016 yılında da alınmıştır ve yeni verilerin analizi de 2016 yılı içindeki hedeflerden biridir. Yeni kalibrasyon katsayıları, yeni veri alım dönemindeki çarpışma analizlerde kullanılacaktır.

Bu işlerin yanı sıra 2016 yılı içerisinde devam eden çevrimiçi yazılım, HF fiberleri radyasyon hasarı izleme görevleri devam etmektedir. Çevrimiçi yazılım yükseltme görevi, yeni nesil veri okuma modüllerinden veri alınmasını sağlayan yazılım paketinin geliştirilmesini içermektedir. Adı ngRBXManager olan yazılım paketi, yeni nesil zamanlama kontrol modülüyle (ngCCM) haberleşerek algıcın elektroniğinden verilerin alınmasını sağlayan pakettir. Bu pakette hangi yükseltmelerin yapılacağını belirlemek de görevin bir parçasıdır. HF kalorimetresi radyasyon hasarı izleme görevi, sürekli olarak algıç üzerinden alınan verilerle kalorimetrede yer alan fiber kabloların hasarını belirlemek içindir. Veriler lazer aracılığıyla özel hazırlanmış 56 HF kanalından alınır. Bu veriler CMSSW yazılım paketi aracılığıyla analiz edilerek zaman içerisinde radyasyon hasarı izlenmektedir. HF çalıştığı sürece radyasyon hasarı olacağından dolayı bu görev dönemlik değil, sürekli yapılması gereken bir iştir.

1. INTRODUCTION

Question of “What is the building block of matter?” has become the most important question of humankind for centuries. This question dates back to BC 600. At those years, it was common that matter is made of particles. Etymologically, ancient Greek philosophers such as Leucippus, Democritus and Epicurus worked on “atom” which means “indivisible.”

In 19th century John Dalton claimed that elements are made of particles which are called atoms [1]. Through the end of the century, physicists started to discover atoms and what is in it. With discovery of quantum and nuclear physics, fusion and fission in the beginning of 20th century, atom which was thought to be indivisible was divided. While technology and science were growing up, new particles started to be observed.

First observed particle was electron with J. J. Thomson’s cathode tube experiment in 1897 [2]. Ernest Rutherford discovered atom in 1911 and proton in 1919 [3]. In 1928 Paul Dirac proposed positively charged electron and it was discovered in 1932 by Carl D. Anderson at California Institute of Technology (Caltech) via cosmic ray experiments and it is named positron [4, 5]. In 1937, Seth Neddermeyer, Carl D. Anderson, J. C. Street and E. C. Stevenson discovered a muon in cosmic ray experiments; nevertheless, its existence was proven by cloud chamber experiment of J. C. Street and E. C. Stevenson in 1937 [6]. In 1947, George Dixon Rochester and Clifford Charles Butler discovered kaon in cosmic rays at Manchester University [7]. For photon, it is hard to give a name and a date about its discovery.

In 1953, accelerator era started by Brookhaven National Laboratory’s (BNL) 3.3 GeV accelerator whose length is 72 m. In 1955, anti-proton was discovered by Owen Chamberlain, Emilio Segre, Clyde Wiegand and Thomas Ypsilantis at 6.2 GeV Bevatron in Berkeley [8].

Later, in 1956 Frederick Reines and Clyde Cowan discovered electron neutrino at Los Alamos reactor [9]. In 1962, Leon Lederman, Melvin Schwartz and Jack Steinberger found muon neutrino [10]. In 1954, strange particles were discovered at Bevatron. Charged cascade particle whose strangeness number is two, was observed in cosmic rays at Manchester University in 1952, and neutral cascade particle was discovered in 1959 in Berkeley.

In 1969, quarks were observed during proton-electron collisions at Stanford Linear Accelerator Center (SLAC). Up, down and strange quarks were observed at SLAC [11]. Charm quark was independently discovered by Burton Richter team at SLAC and Samuel Ting team at BNL [12, 13]. Bottom or beauty quark was observed by Leon Lederman team at Fermi National Accelerator Laboratory (FNAL) and top quark was discovered by The Collider Detector at Fermilab (CDF) and D∅ collaborations at FNAL in 1995 [14–16].

In 1979, gluons were indirectly discovered at German Electron Synchrotron (DESY) and in 1983, The Underground Area 1 (UA1) collaboration at The European Organization for Nuclear Research (CERN) discovered $W^{\pm}$ and Z^{0} bosons with Carlo Rubbia and Simon van deer Meer [17–19].

On July 4, 2012 CERN announced discovery of a new particle which had five sigma level signal for Higgs boson [20]. On March 14, 2013 the particle which was observed in July was announced as Higgs boson in Moriond Conference by analysis of 2.5 times more data by Compact Muon Solenoid (CMS) and A Large Toroidal Large Hadron Collider Apparatus (ATLAS) collaborations [21].

Hadrons are composite particles rather than fundamental particles. Hadrons which are composed of two quarks are called mesons and hadrons composed of three quarks are called baryons.

Particle physics sometimes called high energy physics. The reason why it is called high energy physics is not because of macroscopic energy level of protons, it is because higher energy density of protons compared to their mass and volume. There are two types of interaction as decay and scattering. Collision of two or more particles (and eventually production of new particles) is called scattering. Division of one particle into two or more particles is called decay.

2. PARTICLE PHYSICS

Particle physics is a branch of physics which is related to particles and interactions between each other as well as radiation and fundamental particles. Mostly it is called high energy physics, because particles need to be collided with other particles at higher energy in order to produce and observe the fundamental particles.

2.1 Standard Model

Standard model is the most realistic model that explains particles and interactions between the particles. However, it does not show us the whole picture of the universe. It includes three particle families called leptons, quarks and force carriers.

Leptons have three generations to include electron, muon and tau, and three neutrinos corresponding to these three leptons. First generation consists of electron and electron neutrino, second consists of muon and muon neutrino, and third consists of tau and tau neutrino (Table 2.1). Each lepton has different combination of charge, mass, electron number, muon number and tau number. Each lepton has anti-particle called anti-leptons. Anti-leptons have opposite charge and opposite lepton number to the corresponding leptons. Leptons are fermions, since their spins are $1/2$.

Table 2.1 : Properties of leptons.

leptons	symbol	electric charge	mass
electron	e^-	-e	$0.511\ MeV/c^2$
electron neutrino	ν_e	0	$< 2\ eV/c^2$
muon	μ^-	-e	$106\ MeV/c^2$
muon neutrino	μ_ν	0	$< 0.19\ MeV/c^2$
tau	τ^-	-e	$1.78\ GeV/c^2$
tau neutrino	ν_τ	0	$< 18.2\ MeV/c^2$

Quarks have three generations also. Each generation includes two quarks as up (u) and down (d) quarks, strange (s) and charm (c) quarks, and bottom (b) and top (t) quarks, respectively (Table 2.2). Each quark has anti-particle called anti-quark. Anti-quarks have opposite electrical charge and opposite color charge to corresponding quarks. They are also fermions, since their spins are $1/2$.

Table 2.2 : Properties of quarks.

quarks	symbol	electric charge	mass (MeV/c^2)
up	u	2e/3	1.5-3.0
down	d	-e/3	3-7
strange	s	-e/3	95 ± 25
charm	c	2e/3	$1.25 \pm 0.09 \times 10^3$
bottom	b	-e/3	$4.20 \pm 0.07 \times 10^3$
top	t	2e/3	$174 \pm 3.3 \times 10^3$

Force carriers or mediators are spin-1 particles; hence, they are bosons. Each fundamental force has different force carrier. For gravity, force carrier is hypothetical graviton and hasn't been observed yet, and it is also not included in standard model. Force carrier for electromagnetism is massless photon. Strong force has eight different colorful gluons as force carriers. Neutral Z^0 and charged $W^{\pm}$ bosons are the force carriers of weak force. These particles have mass unlike other bosons. There is another extra boson called Higgs boson which explains the masses of $W^{\pm}$ and Z^0 bosons (Table 2.3).

Table 2.3 : Properties of force carriers and Higgs boson.

force	force carriers	charge	mass (GeV/c^2)	spin
strong	gluons	0	0	1
electromagnetic	photon (γ)	0	0	1
weak (charged)	$W^{\pm}$	± 1	80.4	1
weak (neutral)	Z^0	0	91.2	1
-	higgs	0	125	0

2.2 Particle Dynamics

There are four fundamental forces in nature. These forces are gravity, electromagnetism, strong interaction and weak interaction. Combining electromagnetism and weak interaction, S. L. Glashow, A. Salam and S. Weinberg won the 1979 Nobel Physics prize with their Glashow-Weinberg-Salam model [22]. These fundamental forces have different ranges and strengths. While coupling constant for strong force dramatically increases in short distance, for other forces coupling constant decreases in short distances. This also explains why quarks cannot be observed as single. When quarks are tried to be separated from each other, coupling constant drastically increases and more energy is required to separate quarks from each other. Even if there is enough energy to separate quarks, this intense energy will produce new quark couples immediately. The reason why quarks cannot be seen as a single quark is that the energy needed to separate quarks will turn into mass creating a new quark.

2.2.1 Electromagnetic force

James Clerk Maxwell combined electric and magnetic forces with his book named "A Dynamical Theory of Electromagnetic Field" as electromagnetic force in 1864. With his addition to Ampere's law, he showed that changing electrical field produces magnetic field. Combining this law with Gauss' laws and Faraday's induction law, he formed Maxwell equations for electromagnetism (Table 2.4).

Table 2.4 : Maxwell equations.

Law	differential form	integral form
Gauss' law	$\Delta.E = \frac{\rho}{\varepsilon_0}$	$\oint_s E.dA = \frac{Q}{\varepsilon_0}$
Gauss' law for magnetic field	$\Delta.B = 0$	$\oint_s B.dA = 0$
Faraday's induction law	$\Delta \times E = \frac{-\partial B}{\partial t}$	$\oint_s E.dl = \frac{-d\varphi_B}{dt}$
Ampere's law	$\Delta \times B = \mu_0 J + \mu_0 \varepsilon_0 \frac{\partial B}{\partial t}$	$\oint_s B.dl = \mu_0 I + \mu_0 \varepsilon_0 \frac{-d\varphi_E}{dt}$

First Maxwell equation is Gauss' law which explains that source of electrical field is electrical charge. Second equation indicates that there is no source for magnetic field meaning that there is no magnetic monopole. Third law is Faraday's law which shows that changing magnetic field forms an electrical field. Fourth and the last law is Ampere's law and Maxwell showed that changing electrical field produces magnetic field adding a new term which is the actual contribution of Maxwell. This set of four equations explains all phenomena about electromagnetism. These equations are also invariant under Lorentz transformation.

Electromagnetic force acts on particles decreasing by inverse square of distance to the source and it has an infinite range. Force carrier of electromagnetism is spin-1 photons which have no mass and no charge. Anti-particle of a photon is photon. Photons are emitted from accelerated particles and propagate with the speed of light. In electromagnetic spectrum, gamma rays, X-rays, ultraviolet, visible light, infrared, microwave and radio waves are all photons in different energies and wavelengths.

2.2.2 Strong force

After well understanding of electromagnetism, next question was about how protons stay together in an atom's nuclei. According to electromagnetism, particles with the same sign of charge have to repulse each other, and this repulsive force has to be way much higher at subatomic scale due to inverse square law of electromagnetism. This phenomena can be explained by introducing a new force of nature. Strength of this force has to be higher than electromagnetism and its range has to be too short so that it cannot be felt from outside of the nuclei. This force is strong nuclear force which loses its effect below 10^{-15} m range.

This force acts on quarks which have color charges. Therefore, it acts on baryons which are made of three quarks and mesons which are made of two quarks. Proton and neutron are baryons with three quarks, and pion and kaon are mesons with two quarks. All hadrons are colorless. These color charges are just an analogy with red, blue and green. Each of these colors have an anti-color as anti-red, anti-green and anti-blue. In nature, combination of these three colors is white, that is, colorless. Therefore, in baryons each quark has three different colors. Mesons have quark anti-quark couple which makes them colorless.

In strong force, there are gluons carrying one color and one anti-color charge as force carriers. Nine different unique combinations can be generated by three color and three anti-color charges. These nine combinations are sum of singular and octet combinations. Singular combination is colorless. Singular combination is prohibited, since colorless combination can interact with only colorless combination and there are no long distance gluon interactions. In octet combinations there are eight bicolor gluons that can interact with each other.

2.2.3 Weak force

Weak force is responsible for subatomic decay. Force carriers of weak nuclear force are W^+, W^- and Z^0 bosons. These particles have huge mass unlike gluons and photons (Table 2.3).

While particle flavor is being conserved for other forces, it is not conserved for weak nuclear force. For example, up quark can turn into charm quark by emitting a Z^0 boson.

Probabilities of these translation are given by 3x3 Cabibbo-Kobayashi-Maskawa matrix which is experimentally determined. Since weak force does not interact with color charge, color charges of quarks are conserved. Electron can turn into an electron neutrino by emitting W^-. However, generations are conserved for leptons. For example, in a weak interaction including electron and electron neutrino, a lepton from muon or tau generations cannot be observed. In other words, lepton numbers are conserved for weak interaction.

3. EXPERIMENTAL PARTICLE PHYSICS

Experimental particle physics aims to observe particles and interactions between particles. For this purpose, physicists need detection devices such as accelerators and detectors. Accelerator is the device which supplies accelerated particles to be collided and observe emerging particles. When a collision happens with particles accelerated by an accelerator, sensitive and faster detectors need to determine and identify those emerging particles.

3.1 Accelerator Physics

Subatomic particles usually cannot be observed easily, since their lifetimes are mostly way much shorter than a second. With specified arrangements called "particle accelerators" which are designed for this purpose, particles accelerated by high electrical field are being focused for collision to produce new particles, and then these secondary particles are observed and identified.

After Rutherford’s atomic model in the beginning of 20th century humankind’s searches and interests for solving fundamental structure of matter have led to the usage of accelerated particles such as electrons and protons for new particle physics and nuclear physics experiments. First experimental studies started in 1920s, varied in 1930s and beam energies increased 10 times in each 7 years starting from late 1940s. Today we have an accelerator at 13 TeV, The Large Hadron Collider (LHC). Accelerators which have become inevitable experimental devices of particle physics and nuclear physics, (alongside main purposes such as producing fundamental particles, secondary beams, and especially fundamental researches) have had roles on various science and technology sector about producing industrial and technological products, and have helped development of macro economy, engineering and technology in developed countries.

When the accelerator centers, such as CERN at Swiss-French border, DESY in Germany, The High Energy Accelerator Research Organization (KEK) in Japan, SLAC and FNAL in United States of America (USA), Novosibirsk and Protvino Accelerator Centers in Russia where in each of them hundreds of PhD people work considered, development of countries can easily be noticed in fields of information, technology and engineering.

Accelerators are widely used from particle physics and nuclear physics experiments to material physics, from X-rays to neutron therapy, from proton therapy to ion implantation, from searching for fuel and gases to elimination of environmental waste, from sterilization of food to isotope production, from cleaning of nuclear waste to thorium reactors, from polymerization to lithography, from angiography to cleaning of sera gases, from micro spectroscopy to power electronics, from synchrotron radiation to free electron lasers, from heavy ion fusion to plasma heat. Isotopes or metallic surfaces which are resistant to rusting for 15 years produced by ion implantation that are worthy thousands of dollars are just few example products of accelerators.

Large number of researches about physical, chemical and biological substances in synchrotron radiation laboratories which are based on electron accelerators such as Hamburg Synchrotron Laboratory (HASYLAB) in Hamburg, Berlin Electron Storage Ring Society for Synchrotron Radiation (BESSY) in Berlin, European Synchrotron Radiation Facility (ESRF) in Grenoble, Elettra Sincrotrone Trieste (ELETTRA) in Trieste etc. would be perfect indication of growing application of micro technologies and investment to these applications.

Today there are more than 15,000 accelerators at varying scales all around the world. Around 7,000 of these accelerators are used in ion implantations and surface modification, 1,500 of these are used in industry, 1,000 of these are used in non-nuclear researches, 5,000 of these are used in radiotherapy, 200 of these are used in medical isotope production, 20 of these are used in hadron therapy, 70 of these are used as synchrotron radiation source. Number of large scale accelerators for particle physics experiments, nuclear physics experiments, production of synchrotron radiation and electron laser and developing new technologies which are mentioned earlier are about 110. They have many impact on technology, science and economy. For example, today at CERN, there are more than 14,000 scientists working from hundreds of institutes in more than 100 countries.

Idea of atom dates back to Democritus. Starting from Curie's discovery of radioactive elements such as radium and polonium, atomic physics led to nuclear physics with J. J. Thomson's discovery of electrons and E. Rutherford's experiment of atomic structure. Recent researches are related to more fundamental particles which makes up nucleus. These researches are done at national and international laboratories such as CERN and FNAL. They have many effects to daily life such as hadron therapy as well as internet.

3.1.1 The Large Hadron Collider

The Large Hadron Collider (LHC) is the biggest particle accelerator at CERN near Geneva,Switzerland. LHC is a 27 km long circular accelerator to accelerate particles up to 7 TeV.

LHC sits at Large Electron Positron Collider (LEP) tunnel. Exact circumference of tunnel is 26,659 m. There are more than thousand magnets around the 27 km ring that is about 100 m underground. Around the ring, there are 8 points to reach underground (Figure 3.1). In the LEP era, there were 4 experiments which sat at 4 different points around the ring, the point 2, 4, 6 and 8. Their name were L3, ALEPH, OPAL and Detector with Lepton, Photon and Hadron Identification (DELPHI), respectively (Figure 3.2).

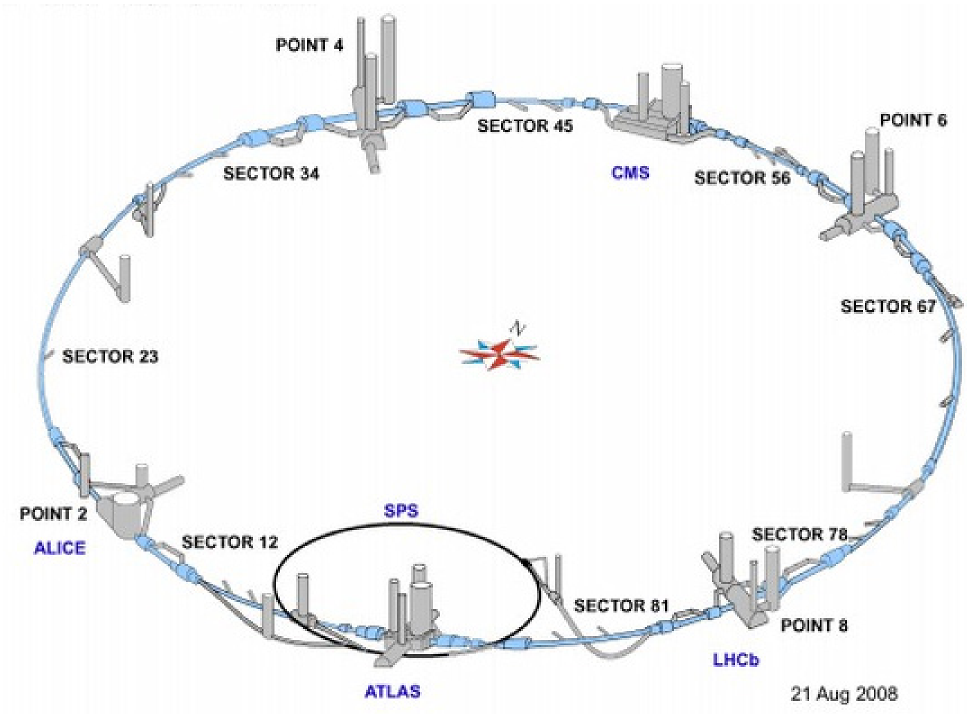

Figure 3.1 : LHC plan with access points and sector names. There are 8 access points to go down the tunnels and experiments.

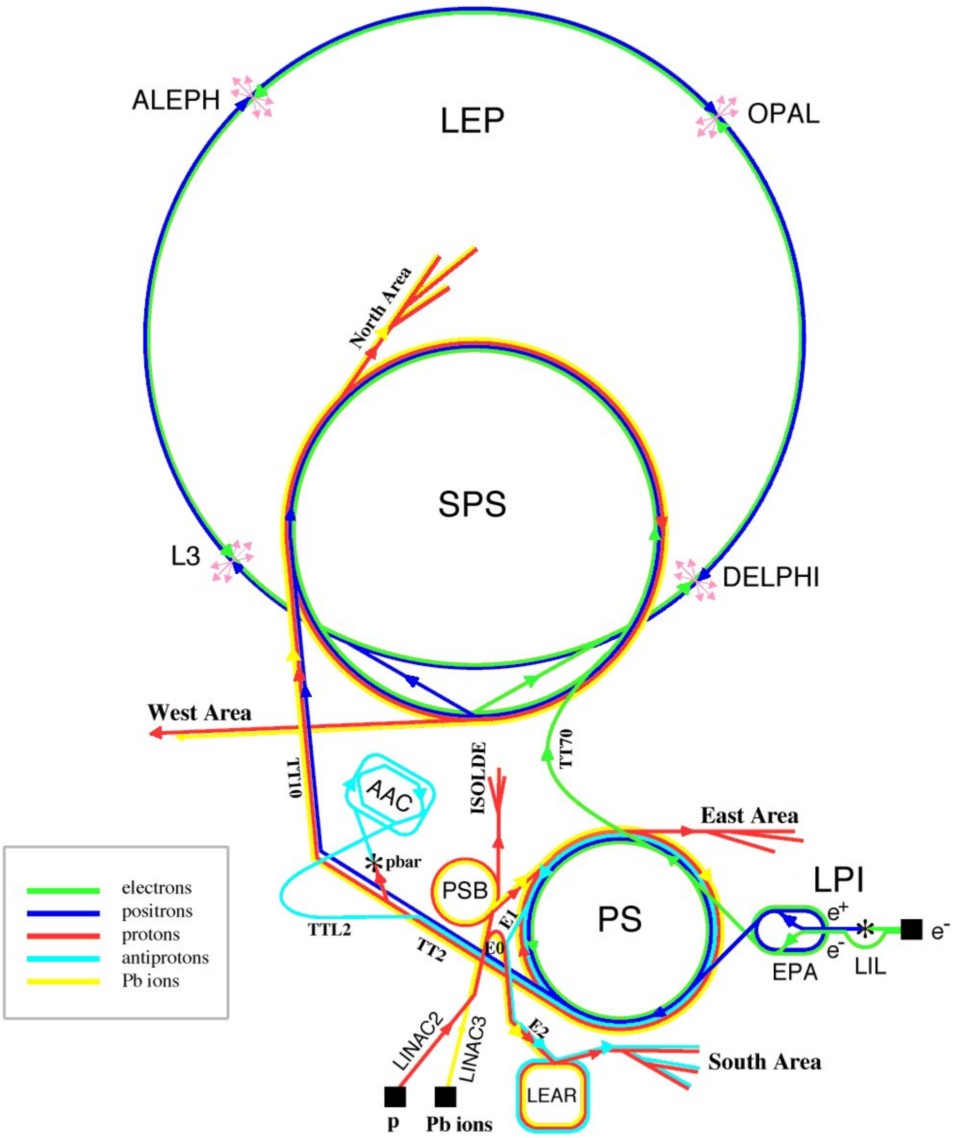

Figure 3.2 : LEP era experiments and CERN accelerator plan. There were 4 LEP experiments at 4 different points.

At point 1 which is just across the CERN main campus in Meyrin village near Geneva, ATLAS experiment sits. New cavern started to be built in 1999 for ATLAS experiment. Point 2 which housed L3 experiment was replaced by A Large Ion Collider Experiment (ALICE) experiment. Point 3 is just an access point to LHC/LEP tunnels. ALEPH experiment was removed from point 4 and now it is used as access point to LHC tunnels and accelerating cavities. At point 5, two new caverns have been built for CMS detector and excavation started in 1999. In one of these caverns, CMS itself lies. Other cavern is just for service with full of electronics and cryogenics systems. First control room of CMS was in service cavern, then it was moved to the surface of point

5. OPAL experiment was removed from point 6; therefore, point 6 and 7 are access points to LHC tunnels. DELPHI experiment was replaced by LHCb experiment.

Large Hadron Collider is made of several components. It consists of 1,232 dipole magnets, several hundred quadrupole magnets and 16 accelerating cavities. Dipole magnets are 15 m long and weighs 35 tones. Dipole magnets include 2 individual beam pipes where particles travel in opposite directions. Beam pipe radii are around 2 cm. Around the pipes, there are steel pipes for vacuuming. Vacuum is up to 10^{-9} mbar. Liquid helium is used to cool down magnets up to 1.9 K temperature. Liquid helium is isolated with 2 small pipes inside the beam pipes (Figure 3.3).

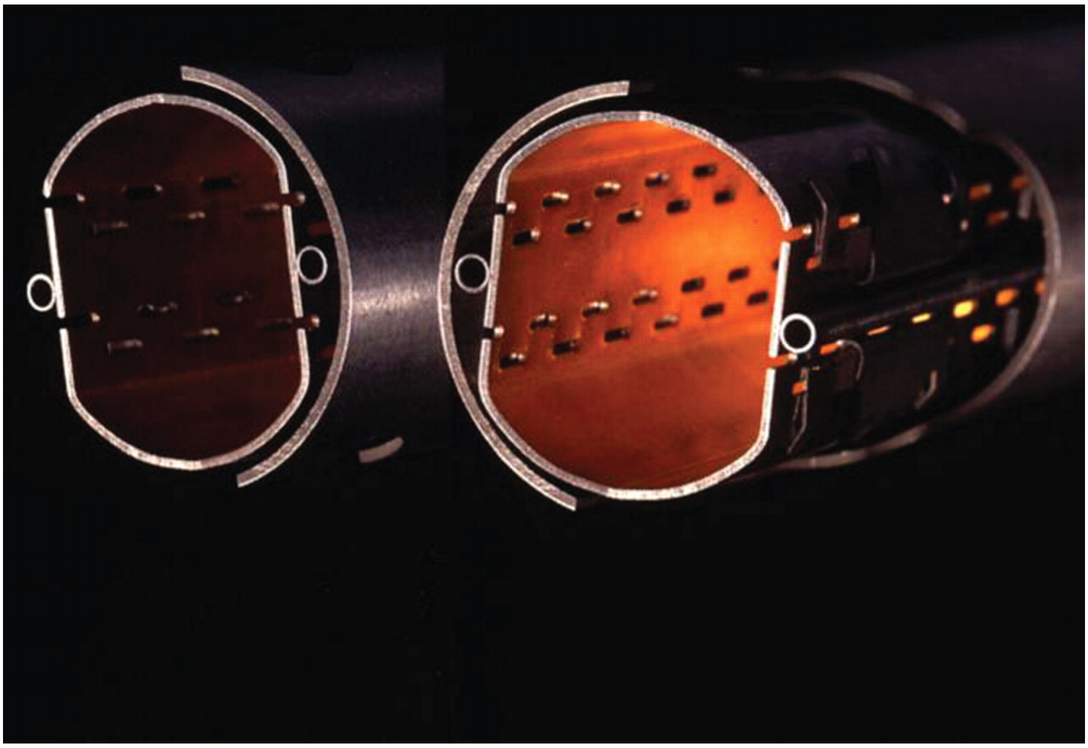

Figure 3.3 : LHC beam pipes. Accelerated particles are flowing at center of these beam pipes in opposite directions. Small pipes above and below of beam pipes are liquid helium pipes for cooling the magnets and beam pipes.

Liquid helium pipes also cool superconducting coils around the beam pipes. Superconducting filaments are made of niobium-titanium alloy (NbTi). They are designed to carry 13 kA current to produce 8.33 Tesla peak magnetic field which makes them the most powerful magnets ever made. Critical temperature of niobium titanium is 9.2 K; however, in order to be able to make it carry 13 kA current, it needs to be cooled till 1.9 K. These magnets are powerful enough to bend 7 TeV protons to 27 km long ring. Magnetic field is set to have vertical lines inside beam pipes (Figure

3.4). This will allow to bend particles towards center of accelerator by Lorentz force applied on particles. Since magnetic field lines will be in opposite direction for two pipes, particle beams will be bent together towards the center of accelerator.

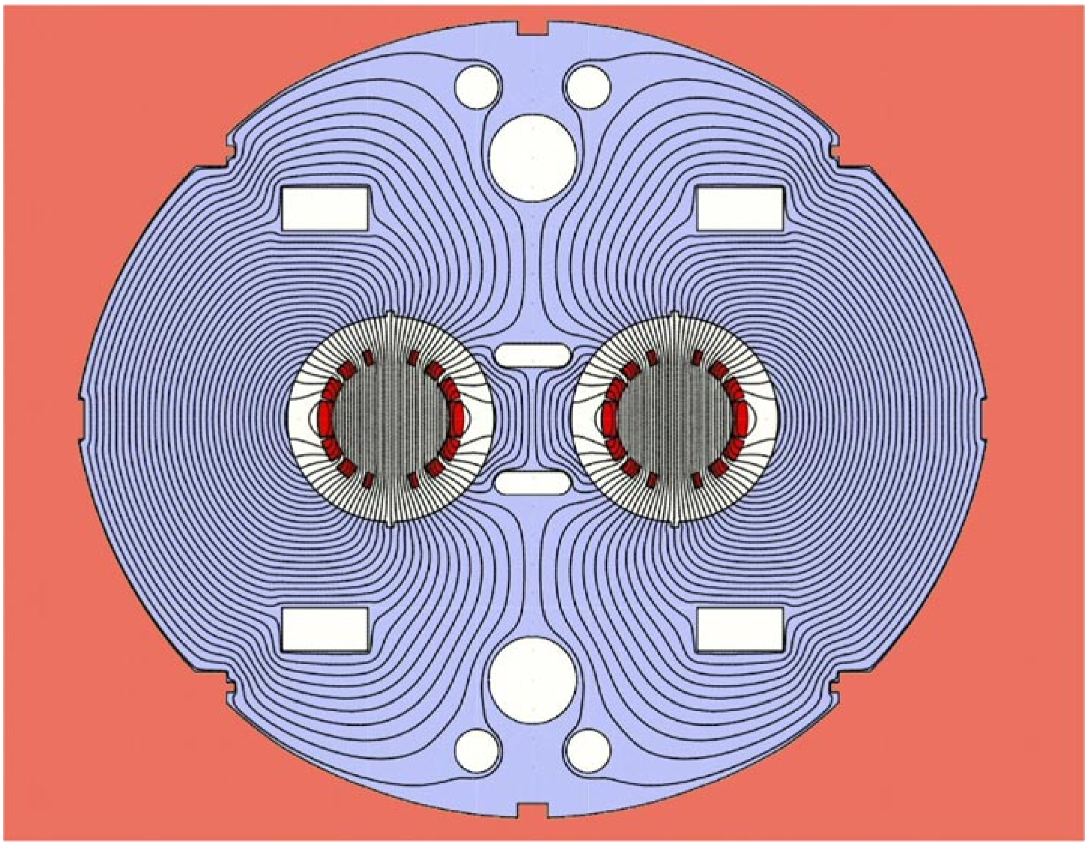

Figure 3.4 : Magnetic field curves of LHC dipole magnets. Magnetic field curves are just straight vertical lines inside beam pipes, and they are in opposite direction inside the pipes.

LHC is also equipped with quadrupole magnets. Quadrupole magnets are relatively smaller than dipole magnets, almost half the size. They also have white covers unlike blue dipole covers. Depending on polarization, quadrupole magnet can focus particles either vertically or horizontally. When a beam is focused both vertically and horizontally, beam will be localized to a very small radius. This will prevent beam to spray around. These quadrupole magnets are distributed around the ring.

Accelerating cavities sit at point 4. In total, there are 16 radio frequency (RF) accelerating cavities in 4 cylindrical tubes called cryomodules, two cryomodules per beam pipe. Each radio frequency generator oscillates at 400 MHz to accelerate particle beam. They can conduct 2 MV per cavity which makes 16 MV in total per particle beam.

3.1.2 Sub accelerators of The Large Hadron Collider

LHC has sub accelerators to accelerate particles nearly to the speed of light (Figure 3.5). A hydrogen tube is used for proton source. Since beams are not continuous, 2×10^{-9} g hydrogen is being taken per bunch of protons. After taking hydrogen atoms to duoplasmatron, protons and electrons are separated. Then protons are boosted at linear accelerator 2 (LINAC2) through The Proton Synchrotron Booster (PSB). The highest energy of protons at LINAC2 is 50 MeV and speed is around 31.4% of the speed of light. After injection to the PSB, protons circulate inside 4 different cycles. The highest energy and speed in PSB are 1.4 GeV and 91.6% of the speed of light.

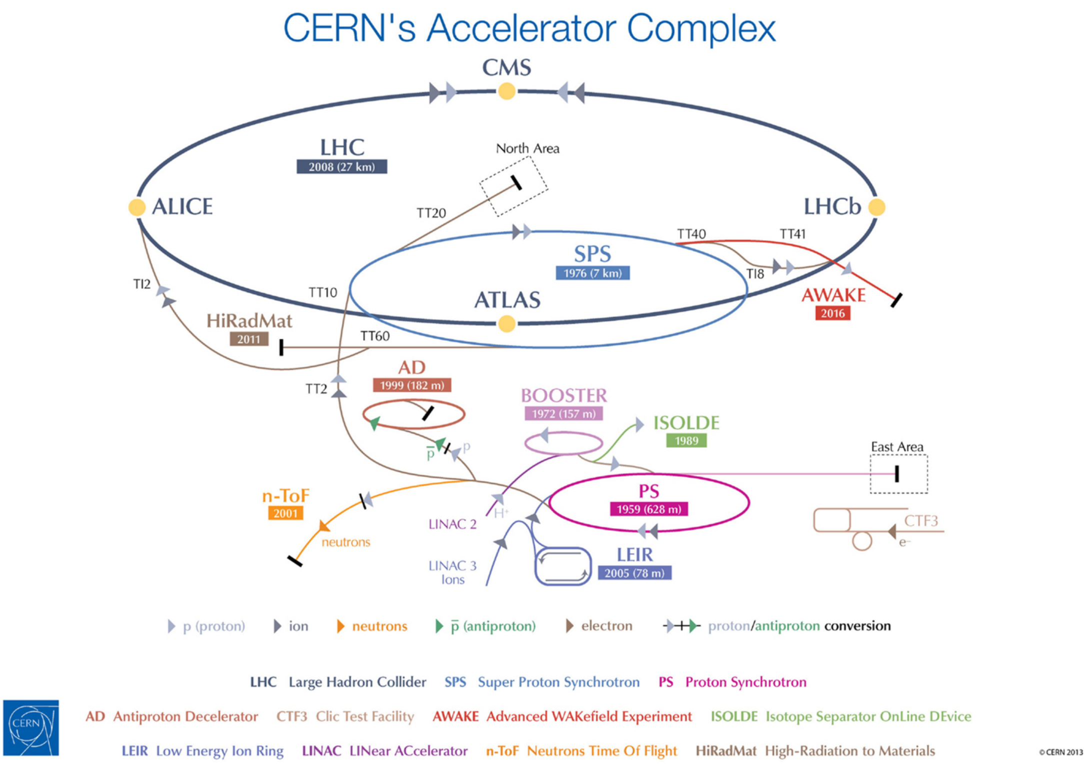

Figure 3.5 : CERN accelerator network. There are several subcycles of LHC to accelerate the particles nearly to the speed of light.

Next cycle for particle beam is The Proton Synchrotron (PS) which is one of the very first accelerators at CERN. In PS, maximum energy of protons is 25 GeV, and maximum speed is 99.93% of the speed of light. Length of PS is around 628 m in a circular geometry.

When protons have enough energy and speed, they are ready to be injected to The Super Proton Synchrotron (SPS) which is 7 km long circular accelerator. Protons will gain energy up to 450 GeV and speed up to 99.9998% af the speed of light.

Last cycle will be LHC after a pilot beam injection. Pilot beam is being injected to LHC to check whether it would be circulating around the ring. If everything is working fine, proton bunches are being injected into the LHC beam pipes in opposite direction. LHC can accelerate protons up to 99.9999991% of the speed of light. Initial designed energy of LHC is 7 TeV per beam which will make 7 TeV + 7 TeV = 14 TeV center of mass energy when a collision happens. In the first experimental period called run-1, LHC could reach up to 3.5 TeV and 4 TeV per beam meaning that 7 TeV and 8 TeV center of mass energy collisions. After long shutdown 1 (LS1) phase, LHC could reach to 6.5 TeV per beam corresponding to 13 TeV center of mass energy collisions in 2015. 13 TeV collisions will continue during 2016.

3.2 Detector Physics

It is not necessary "to see" to be able to observe something. The simplest example would be the wind which we can't see it, but we can feel. However, seeing is not enough in scientific methods. Results have to be saved and it is shared with the public. For example, in photography you can see an object, but in real you just see tracks of the object in the photograph. In this context, seeing subatomic particle means seeing tracks of the particles Therefore, detection is more important than seeing something. In general, seeing a particle and observing its interaction mean recording its energy (E), momentum (p), charge (q) and/or spin (s) by measurements. Detectors are such a device which can detect and record these properties.

3.2.1 Cloud chambers

Wilson won 1927 Nobel Physics award with a detector he invented the cloud chamber. It was especially used by experiments between 1920-1950. It is just a supersaturated alcohol steam in a closed volume, that is why it is called a chamber. Particles in the chamber ionize alcohol vapor; hence, ionized alcohol becomes visible as cloud. Each tracks are recorded to be analyzed later. If a magnetic field is applied to the chamber, charged particles will be curved due to Lorentz force. Using its curvature, momenta and charge of those particles can be measured. Thanks to this invention positron, muon and kaon were observed in 1932, 1937 and 1947, respectively [5–7].

3.2.2 Bubble chambers

Bubble chambers have been invented by Glaser in the beginning of 1950s and he has won 1960 Nobel Physics award. It basically consists a cylinder or sphere full of liquid. Liquid is kept just under boiling temperature with a certain pressure and temperature, i.e. liquid hydrogen at 27 K temperature and 5 bar pressure. When a particle reaches the chamber, pressure is suddenly lowered, i.e. from 5 bar to 3 bar. Charged particles lose their energy by ionizing the matter. This causes non-stable liquid to vaporize and produces bubbles. Photographs are taken in 1 or 2 ms. Multiple cameras provide more resolution up to 10 μm. It can be bigger than cloud chambers and can detect more energetic particles since it includes denser liquid. Gargamelle and The Big European Bubble Chamber (BEBC) are the two examples. Gargamelle experiment at CERN discovered weak neutral currents.

3.2.3 Compact Muon Solenoid experiment

Imaging interaction of beam is required for recording and statistics. Only interesting events need to be studied. Most of the events produced by an interaction of a beam bunch are already known. That is why studying all events would be a waste of time. Elimination of those events requires a filtering. Before, those filtering was being done by hand, but now it can be done by electronics and software.

Today, bigger detectors consists of several parts to observe properties of particles and interactions. Since different particles have different effects on different materials, detectors can be more effective using the most effective materials.

CMS experiment is one of the bigger detectors of LHC at CERN. LHC houses 4 different giant detectors called CMS, ATLAS, ALICE, LHCb. ALICE and LHCb experiments are relatively smaller than CMS and ATLAS experiments. They are looking for specific physics. While ALICE is looking for quark-gluon plasma –state of matter just after Big Bang–, LHCb is interested in about matter anti-matter asymmetry or CP violation. CMS and ATLAS experiments are bigger experiments which are looking for any signs of new physics. They are called general purpose detectors. The reason why there are two general purpose detectors is to cross check the results. To be able to announce a result as discovery, both of those detectors have to verify their results as in the Higgs boson discovery in 2012. They are designed in a completely different structure in order not to have same systematical problems as well as to increase statistics. For example, while CMS has only one and the most powerful solenoid magnet ever made, ATLAS has a toroid magnet and 3 small solenoid magnets. Even if CMS is not bigger than ATLAS in dimensions, it is the heaviest detector in LHC, weighing 14,000 tones. CMS has 5 slices which all of them have been assembled on the surface during construction of 100 m deep shaft through experimental cavern at point 5. CMS has layers like a cylindrical onion.

The innermost structure of the CMS is silicon pixel tracker to track particles' trajectory. It has many silicon pixel cells which also have inner structure. When a charged particle produced by collisions hits the silicon pixel detector, it can determine the location of the particle. Following those locations through silicon layers, trajectory of the particle can be constructed. Before measuring the energy of particles, it will give a clear track of particle which will allow scientists to find the vertex where they come from.

Next layer is electromagnetic calorimeter (ECAL) which measures energy of electromagnetic particles such as electrons, positrons and photons. Electromagnetic particles deposit all their energy in the ECAL; therefore, it can be understood whether they are electromagnetic particles or hadrons. Once they have been determined that they are electromagnetic particles, they can be identified by using their curvature and their measured energy.

Since hadrons' momentum is higher than electromagnetic particles, they can pass through ECAL and can deposit most of their energy in the hadronic calorimeter (HCAL). That is why HCAL is just after ECAL. As in the ECAL, hadrons deposit all their energy to the HCAL. Electromagnetic particles and hadrons can easily be separated just looking where they deposit all their energy. Those calorimeters can also measure energy of the particles which is one of the most important parameter for identifying particles.

Measuring energy of a particle is not enough to identify a particle. Other parameters should be determined such as charge and momentum. Using Lorentz law, charge of a particle can be found. In the presence of a magnetic field, a charged particle trajectory will be curved. Looking at the curvature of the particle trajectory, charge can easily be determined. Furthermore, mass of the particle can be calculated using radius of curvature, energy and magnetic field. Since mass is unique for all particles, finding mass means identifying the particle.

For that reason, there comes the most powerful solenoid magnet ever made surrounding the HCAL which is “S” in “CMS” acronym. Since particles will have larger momenta, magnetic field has to be powerful enough –around 4 Tesla. CMS scientists decided to use the same superconducting filaments used in LHC magnets, NbTi coils. Critical temperature of NbTi is around 9.2 K. To be able to produce a magnetic field around 4 Tesla in a 6 m diameter and 12.5 m long solenoid, NbTi coils needs to carry around 20 kA current. Solenoid magnet of the CMS would be cooled down to 1.9 K, same temperature as in the LHC via liquid helium. In this case, nominal magnetic field strength will be 3.8 Tesla. This field is enough for bending charged particles' trajectories starting from the tracker layer.

The last layer would be muon chambers, since muons can surpass all layers of the detector –even the muon chambers. Muons are one of the least interacting particle and also have one of the longest lifetime in short lived particle family. CMS detector can detect muons very accurately. Since magnetic field directions are opposite inside and outside of solenoid magnet, curvature of muon tracks will be reversed inside and outside of the magnet (Figure 3.6). Magnetic field strength will be around 2 Tesla in muon chambers.

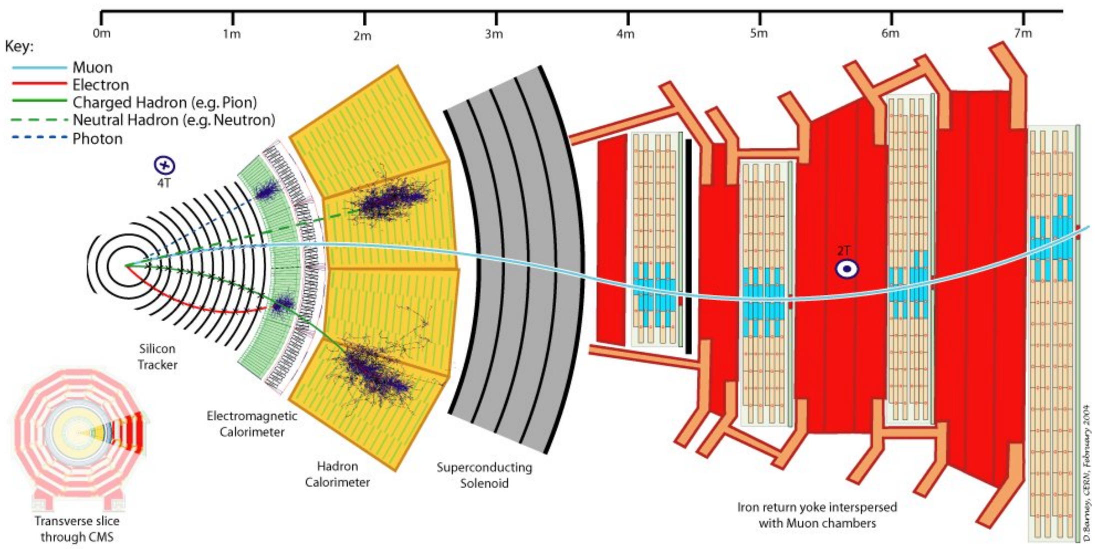

Figure 3.6 : Particle detection in CMS detector. As it can be seen, curvature of muon is different inside and outside of the solenoid magnet.

3.2.3.1 Hadronic calorimeter

HCAL can measure jets and missing transverse energy together with ECAL. HCAL and ECAL will be the complete calorimetry system [23]. Central hadronic barrel (HB) and hadronic endcap (HE) calorimeters of HCAL are immersed with high magnetic field completely surrounding ECAL. HB and HE are connected to each other hermetically and cover $|\eta| < 3.0$ pseudo-rapidity range together. HB covers $|\eta| < 1.4$ and HE covers $1.3 < |\eta| < 3.0$, overlapping range with HB. Hadronic forward (HF) calorimeters that cover $2.9 < |\eta| < 5$,overlapping range with HE, are located 11.2 m from the interaction point. HF calorimeters are designed to detect energetic forward region jets and missing transverse energy to distinguish narrow lateral shower profile. In central part, there is another calorimeter to improve measurement in the range of $|\eta| < 1.26$. This calorimeter is called hadronic outer barrel (HO) and located outside of magnet.

3.2.3.2 Structure of hadronic calorimeter

HB consists of 2 half barrels composed of 18 identical wedges. Each wedge covers 20° in ϕ direction to produce a barrel. Wedges are made of brass alloy absorber plates which is parallel to the beam. Brass alloy consists of 70% copper and 30% zinc. For structural strength, stainless steel is used for innermost and outermost layer. Between brass alloy layer and stainless steel layer, there are 17 active plastic scintillator. First layer directly comes after ECAL. Thickness of this layer is around twice compared to the other layers to sample low energy showering particles from ECAL. Inner radius of HCAL is 1,777 mm and outer radius is 2,876.5 mm. Layers are given by

(Layer 0) 9 mm scintillator/61 mm stainless steel

(Layers 1-8) 3.7 mm scintillator/50.5 mm brass

(Layers 9-14) 3.7 mm scintillator/56.5 mm brass

(Layers 15+16) 3.7 mm scintillator/75 mm stainless steel/ 9 mm scintillator

Layer numbers refer to active scintillator layer. Each scintillator is produced in size of $|\eta| \times |\phi| = 0.087 \times 0.087$ and then assembled with one wavelength shifting fiber (WLS). WLS fibers are connected to clear fibers whose lengths are enough to form 32 barrel towers in η (Table 3.1). There are exceptions for tower 15 and 16, since they have multiple optical readout. Optical signal is read by silicon photomultiplier sensors (SiPM).

HE calorimeter is tapered to connect HB calorimeter and overlap with their tower 16 (Figure 3.7). HE also has 18 wedges made of totally brass absorber plates in ϕ direction matching with barrel calorimeter wedges. Thickness is 78 mm for plates and 3.7 mm for scintillator; thus, it reduces sampling fraction. There are 19 active plastic scintillator layers. ϕ-granularity is reduced to 10° in high η-region (above $|\eta| = 1.74$) because of accommodation of bending radius of WLS fiber readout (Figure 3.8). Because of uniform segmentation, energies are measured in the 10° ϕ wedges and divided equally, and sent to the level-1 calorimetry trigger. $|\eta| \times |\phi|$ is the same between $1.3 < |\eta| < 1.74$; however, η size increases after $|\eta| > 1.74$ (Figure 3.7). HE also includes pseudo-EM part in depth starting from tower 18. This tower is also first tower beyond η coverage of ECAL barrel. First segment of HE is for feeding the regional calorimeter trigger (RCT). Rear segments are for forming hadronic energy inputs for RCT. Rear segments of tower 28 is too large with $\Delta\eta = 0.35$. First two segments of this tower are split in η for precision (Figure 3.7).

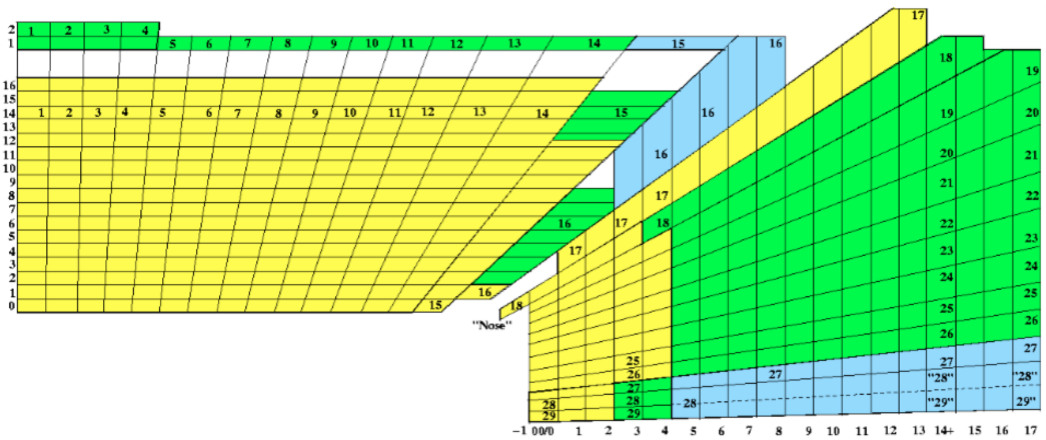

Figure 3.7 : A schematic view of the tower mapping in $r-z$ of the HCAL barrel and endcap regions [24].

Layers of HO calorimeter are outside of solenoid magnet. They are close to the return yoke; therefore, there is muon barrel system just after outer barrel calorimeter. HO consists of 12 sectors in 5 rings each in 2.54 m along z-axis. Ring 0, the central ring, consists of two 10 mm thick scintillator at radial distance 3,850 mm and 4,097 mm, respectively. Other rings only have one layer at 4,097 mm radial distance. All panels are identical except in ring ± 1. Due to chimney structure of magnet, special panels

Table 3.1 : Size of HCAL readout tower in η and ϕ as well as the segmentation in depth. The HF has a non-pointing geometry, and therefore the tower η ranges provided here correspond to $|z| = 11.2$ m [24].

tower	low η	high η	detector	size (ϕ)	size (η)	depth segments
1	0.000	0.087	HB, HO	0.087	5°	HB=1, HO=1
2	0.087	0.174	HB, HO	0.087	5°	HB=1, HO=1
3	0.174	0.261	HB, HO	0.087	5°	HB=1, HO=1
4	0.261	0.348	HB, HO	0.087	5°	HB=1, HO=1
5	0.348	0.435	HB, HO	0.087	5°	HB=1, HO=1
6	0.435	0.522	HB, HO	0.087	5°	HB=1, HO=1
7	0.522	0.609	HB, HO	0.087	5°	HB=1, HO=1
8	0.609	0.696	HB, HO	0.087	5°	HB=1, HO=1
9	0.696	0.783	HB, HO	0.087	5°	HB=1, HO=1
10	0.783	0.879	HB, HO	0.087	5°	HB=1, HO=1
11	0.879	0.957	HB, HO	0.087	5°	HB=1, HO=1
12	0.957	1.044	HB, HO	0.087	5°	HB=1, HO=1
13	1.044	1.131	HB, HO	0.087	5°	HB=1, HO=1
14	1.131	1.218	HB, HO	0.087	5°	HB=1, HO=1
15	1.218	1.305	HB, HO	0.087	5°	HB=2, HO=1
16	1.305	1.392	HB, HE	0.087	5°	HB=2, HO=1
17	1.392	1.479	HE	0.087	5°	HE=1
18	1.479	1.566	HE	0.087	5°	HE=2
19	1.566	1.653	HE	0.087	5°	HE=2
20	1.653	1.740	HE	0.087	5°	HE=2
21	1.740	1.830	HE	0.090	10°	HE=2
22	1.830	1.930	HE	0.100	10°	HE=2
23	1.930	2.043	HE	0.113	10°	HE=2
24	2.043	2.172	HE	0.129	10°	HE=2
25	2.172	2.322	HE	0.150	10°	HE=2
26	2.322	2.500	HE	0.178	10°	HE=2
27	2.500	2.650	HE	0.150	10°	HE=3
28	2.650	2.853	HE	0.350	10°	HE=3
29	2.853	2.964	HF	0.111	10°	HF=2
30	2.964	3.139	HF	0.175	10°	HF=2
31	3.139	3.314	HF	0.175	10°	HF=2
32	3.314	3.489	HF	0.175	10°	HF=2
33	3.489	3.664	HF	0.175	10°	HF=2
34	3.664	3.839	HF	0.175	10°	HF=2
35	3.839	4.013	HF	0.174	10°	HF=2
36	4.013	4.191	HF	0.178	10°	HF=2
37	4.191	4.363	HF	0.172	10°	HF=2
38	4.363	4.518	HF	0.175	10°	HF=2
39	4.518	4.716	HF	0.178	10°	HF=2
40	4.716	4.889	HF	0.173	10°	HF=2
41	4.889	5.191	HF	0.302	10°	HF=2

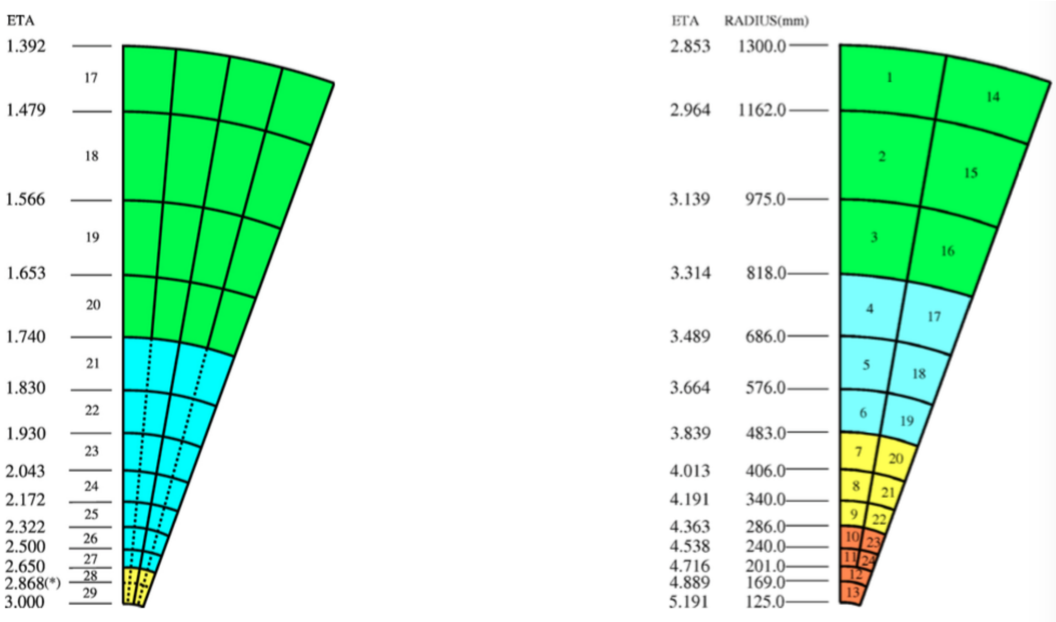

Figure 3.8 : (a) The $\eta - \phi$ view of a 20° HE endcap section showing the 5° regions and "split" 10° regions above $\eta = 1.740$ in detector pseudo-rapidity. The tower 28/29 split in η is also shown. (b) The $r - \phi$ view of an HF wedge (η at $z = 11.2$ m). The shaded regions correspond to the level-1 trigger sums. [24].

have been used with one scintillator row. Pseudo-rapidity coverage of HO is $\eta < 1.26$ except space between muon rings. This space accommodates 75 mm stainless steel support in ϕ direction.

Location of the forward calorimeters are 11.2 m from the interaction point. They consist of steel absorber and hard quartz fiber which can immediately collect Cherenkov light. Each HF section is made of 18 wedges in ϕ direction each having 20°. There are two different length fibers with 5 mm distance, long ones are 1.64 m, short ones are 1.43 m. They are in a bundle and connected to photo multiplier tubes (PMT) separately for readout. η ranges are shown in Table 3.1 and an HF wedge is shown in Figure 3.8.

4. HADRONIC CALORIMETER UPGRADE STUDIES

LHC started first collisions in March 2010. By March 2010, Run 1 started for $\sqrt{s} = 7$ TeV and $\sqrt{s} = 8$ TeV collisions. After Higgs boson discovery in 2012, LHC and all 4 detectors went into the long shutdown 1 (LS1) starting from 2013. $\sqrt{s} = 13$ TeV collisions started in 2015 called Run 2. Around early 2019, Run 2 will be ended and long shutdown 2 (LS2) will be started. During LS2 there will be upgrade phase 1. Run 3 is between early 2021 and late 2023. Phase 2 upgrade –long shutdown 3 (LS3)– will start by early 2024. During LS3, LHC will be upgraded to High Luminosity Large Hadron Collider (HL-LHC) for higher luminosity at $\sqrt{s} = 14$ TeV collisions (Figure 4.1).

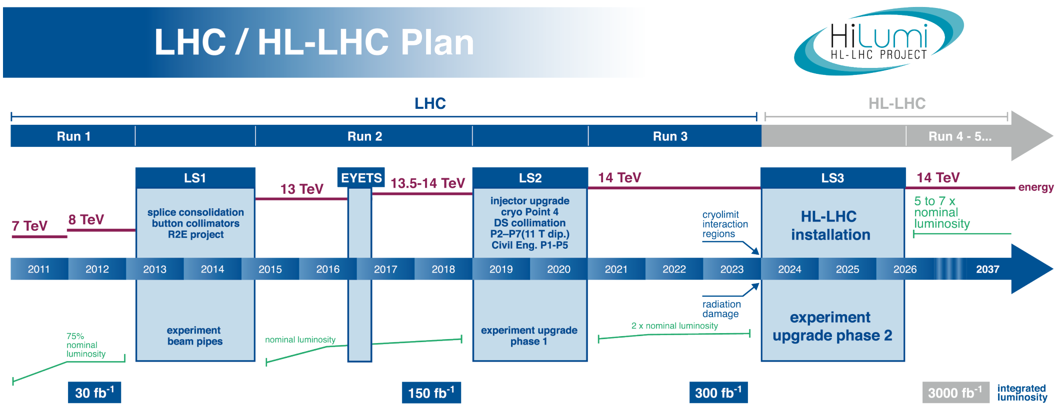

Figure 4.1 : LHC and HL-LHC plan. Run 1 started in 2010 and ended in 2013. During LS1 between 2013 and early 2015, LHC and detectors were upgraded. LS2 is upgrade phase 1 and LS3 upgrade phase 2. During upgrade phase 2 LHC will be upgraded to LH-LHC [25].

In LHC/HL-LHC plan, integrated luminosity will reach 3000 fb^{-1} which will cause radiation damage in detectors. Most parts of the CMS detector were not designed for HL-LHC luminosity. Increasing integrated luminosity will damage detector parts, i.e. scintillators, fibers, photomultiplier, electronics. These parts require replacement before they are damaged to a certain level. When it is considered that integrated luminosity will reach 3000 fb^{-1} by late 2020s, these replacement parts must be stronger against radiation than the old ones.

Hadronic calorimetry group have proposed some upgrades for each subpart of calorimeter –hadronic barrel, hadronic endcap, hadronic outer barrel and hadronic forward calorimeters. Some of these upgrades have been done during LS1 and new upgrades are in process for upgrade phase 1 and upgrade phase 2.

4.1 Upgrade Studies of Hadronic Barrel and Endcap Calorimeters

HE and HB calorimeters consist of brass absorbers and scintillators with WLS fiber readout. There are 17 layers with 72,000 individual scintillators connected to the readout system with individual WLS fibers. The analog inputs coming from the calorimeter are turned into digital data by a minimum number of individual electronics channels, since there are intrinsic signal-to-noise ratio limitations of the WLS light detected by hybrid photodiode (HPD) detectors and corresponding front end noise from readout electronics (Figure 4.2). There is only one depth segmentation readout system for bulk of $\eta - \phi$ barrel segmentation. In endcap calorimeter there is limited depth segmentation, but it is not prepared against high luminosity LHC operation. Several physics analyses done on initial LHC collision have clearly shown areas where they need to be improved. Analysis also have shown that these improvements will directly affect productivity of the experiment. Due to these analysis, areas required upgrades and improvements can be summarized as follows: [26]

1) Need for calorimeter clean-up algorithms to reduce non-collision signals coming from numerous sources,

2) Limited discriminating power of the HCAL/ECAL energy ratio for separating pions from electrons,

3) Degradation of the electron isolation quantities with increasing instantaneous luminosity,

4) Limited efficiency for muon isolation and identification using the HCAL barrel and endcap,

5) Large calibration biases using isolated hadrons below 5 GeV due to showering in dead material between ECAL and HCAL,

6) Inefficient bunch-crossing identification for low-energy signal impacting large area summations used for hardware trigger-level lepton isolation, jet energy and global energy sums,

7) Strong η-dependent radiation damage in the endcap scintillators at high luminosity introducing non-uniform light loss and constant term energy resolution degradation, and

8) Limited number of discriminating quantities to reject beam-related backgrounds not originating from the interaction region.

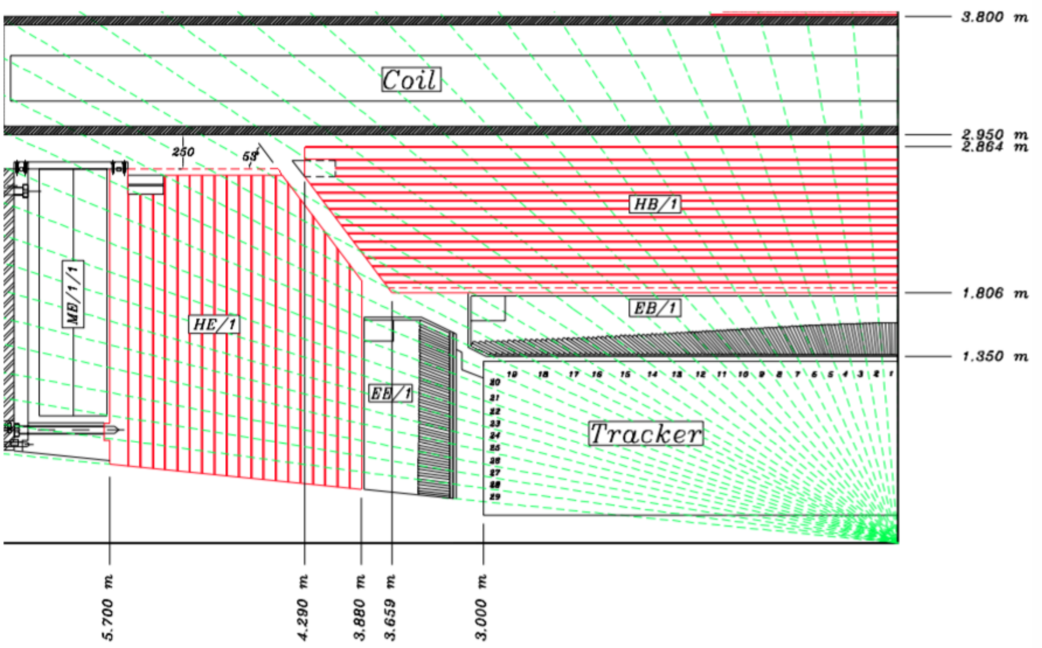

Figure 4.2 : Quarter view of the barrel and endcap hadron calorimeters, showing the intrinsic longitudinal segmentation capabilities. The front-end readout electronics, the readout boxes or "RBX", are located directly behind tower 15 in the barrel and directly behind tower 18 in the endcap [26].

Upgrades and improvements which will overcome these limitations are as follows: [26]

a) Replacement of photodetectors to eliminate the sources of anomalous signals and to improve the front-end signal-to-noise ratio by an order of magnitude,

b) Four-fold increase in longitudinal segmentation to reduce pile-up/high-occupancy performance degradation coming from the first layer of scintillator, to improve clustering and geometric discrimination against non-collision backgrounds and to increase channel redundancy, and

c) Scintillator time, time to digital converter (TDC) measurements per bunch crossing with nanosecond timing resolution down to minimum ionizing particle (MIP) energies to provide independent rejection for beam halo, cosmic ray, and other non-collision backgrounds.

To benefit new upgrades especially for front-end (FE) electronics there are new proposals for back-end (BE) trigger and readout electronics: [26]

1) FE to BE data bandwidth increases from increased longitudinal segmentation and TDC information in the readout of the HB and HE;

2) Data volume management and integration with the central data acquisition (DAQ);

3) Increased trigger processing needs to provide total energy sums, separate lepton isolation quantities and to apply the new FE timing information;

4) Increased bandwidth to the trigger system to provide finer granularity information, including full granularity in the HF region, additional fine-grain information, and separate total energy and lepton isolation sums.

Improvement of HCAL for physics is the main goal of HCAL upgrades. Inherent capability of the HB/HE will be tried to be maximized. Main parameters to improve are high-p_T physics and luminosity beyond 10^{34} cm^{-2}s^{-1} which is LHC design luminosity. For HB and HE calorimeter phase 1 upgrades, modifications to the FE electronics and trigger/readout BE are proposed. FE and BE crates are accessible from outside of the calorimeter, and any modification can be done without modifications of calorimeter. Starting from phase 2, luminosity will be increased to 5×10^{34} cm^{-2}s^{-1}. High integrated radiation level might make defective high η region of HE calorimeter. Improvements on phase 1, such as replacing new technology photodetector and new detector electronics component, can maintain phase 2 performance standard. HCAL and ECAL endcap calorimeter have to look for new components which can maintain high radiation level in phase 2 –in HL-LHC.

According to radiation map of HB and HF calorimeters, they are able to operate at the radiation level of phase 1. Situation is not the same for HE calorimeter. Ionizing radiation will damage HE layers causing less light emittance.

First of all integrated ionization radiation in HE scintillators and in FE readout boxes need to be understood, since radiation will reduce number of photons per GeV. Understanding of ionization and neutron influence are another important parameters for electronics to be able to sit at that environment. HE scintillators are set according to phase 1 luminosity although HE electronics is set according to phase 2 luminosity which is at 5×10^{34} cm^{-2}s^{-1} for 10 years. HE electronics will be able to operate at harsh conditions of phase 2. Also new silicon photomultiplier which were replaced with photomultiplier tubes can operate with the new electronics.

Radiation contours in Grays (100 Rad = 1 Gray) are shown in Figure 4.3 for for 10 years of LHC running at 500 fb^{-1} for HB and HE calorimeter. It can easily be indicated that ionization radiation level is approximately 100 Rad around readout box (RBX) region, and 10 KRad around HB region. These radiation levels are the same with expected radiation levels on LHC phase 1. In the figure, around lower part of HE, radiation level reaches to 1 MRad. Figure 4.4, gives clear understanding of these radiation levels. Around few MRad radiation, scintillator light output will decrease in a significant amount.

In phase 2, expected ionization radiation level will be 10× higher than phase 1; therefore, HE scintillators light output will decrease to few percent, and eventually HE will not be in operation. For that reason, HE scintillators needs to be upgraded by new scintillators for phase 2.

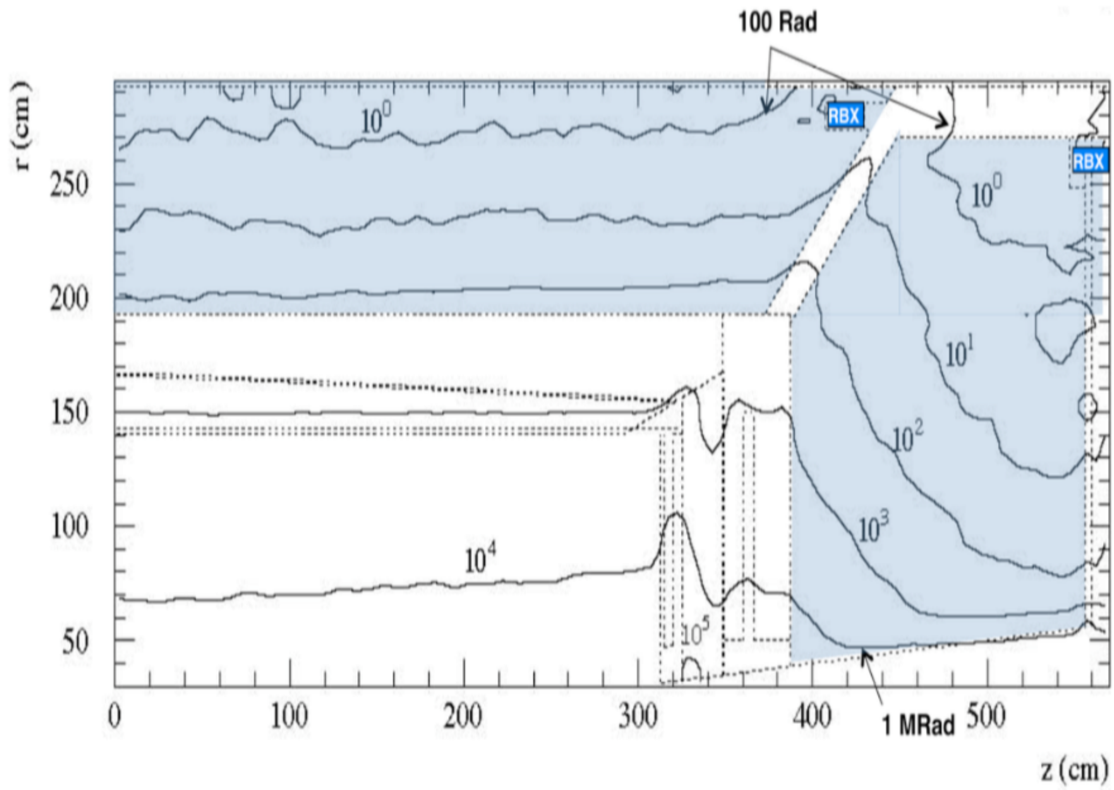

Figure 4.3 : Radiation contours for CMS from FLUKA calculations, units of Grays, after 500 fb^{-1} (10 years at LHC design luminosity). HB and HE begins at $r > 180$ cm and $z >\sim 400$ cm respectively [26].

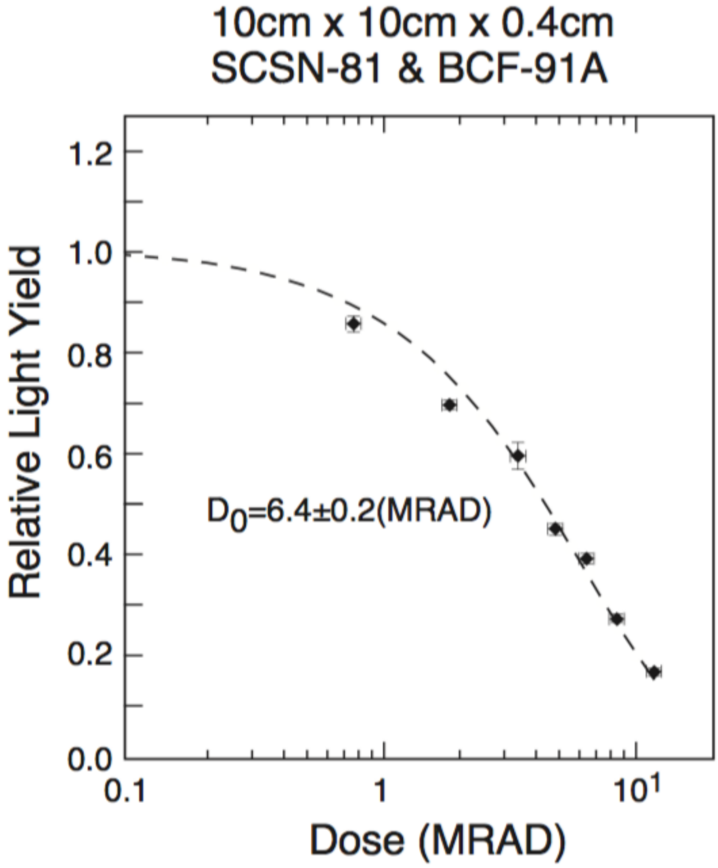

Figure 4.4 : Scintillator radiation damage as a function of ionization radiation [26].

4.2 Upgrade Studies of Hadronic Forward Calorimeters

Forward rapidity calorimeters called HFs consist of quartz fibers for producing Cherenkov light. Cherenkov radiation has an advantage and a disadvantage. The advantage is that it has rapid time response, the disadvantage is that less light is produced by Cherenkov process. Number of photoelectrons per GeV deposited in HF calorimeters is lower than plastic scintillators of HB, HE and HO by two orders of magnitude.

High gain PMTs are used in the HF calorimeters. Radiation level at high rapidity regions will effect PMT window material and ultraviolet (UV) transmission sensitivity of the fiber and light guides. HF can deposit 0.25 photoelectron per GeV energy. Any non-calorimetric interaction with fibers can generate the same level signal as 1 TeV deposited energy.

Each HF calorimeter are made at 36 steel wedges producing a ring with inner and outer radii of 12.5 cm and 120 cm, respectively. They are located 11.2 m from the interaction point and the length of each calorimeter is 1.65 m along beam line. They have 13 segmentation in η and 72 segmentation in ϕ, granularity of $\eta \times \phi = 0.175 \times 0.175$. Photomultiplier tubes read the fiber signal from 864 channels per module and 1728 channels in total.

Well shielded PMTs of HF were produced by Hamamatsu and model name is R7525HA. This model have 8 dynodes, 12.5 mm radius bialkali photocathode, 0.6 cm thick borosilicate silicon window and quantum efficiency (QE) of 22% at 450 nm. The PMTs would be exposed to 8-10 KRad/10 years at 10^{34} $cm^{-2}s^{-1}$ luminosity. The PMT windows will be damaged significantly after 120 KRad.

HF PMT upgrade was proposed to replace Hamamatsu R7525 with new PMTs. Properties of new PMTs are as follows: [26]

1) a thin ($<$ 1 mm) front window that reduces the amount of Cherenkov light;

2) a metal envelope that further eliminates Cherenkov light made by particles traversing the side of the PMT;

3) 45% peak QE; and

4) four-way segmented anodes that allow further rejection of PMT events by using the pattern of light distribution among the anodes, which is different than signals coming from energy deposited in the HF absorber.

Old Hamamatsu R7525 PMTs are replaced by Hamamatsu R7600 PMTs which provides all the properties listed above (Figure 4.5).

Figure 4.5 : New photomultiplier tubes of HF wedges. Hamamatsu R7600.

5. EXPERIMENTATION AND ANALYSIS

5.1 Hadronic Endcap Calorimeter Scintillator Upgrade

Hadronic endcap calorimeter scintillators are not designed for phase-2 operations and require replacement with stronger scintillator material against radiation. For that reason, many scintillators are proposed by 4 different institutes, Maryland University (UMD), Iowa University (UI), FNAL and Dubna (Table 5.1).

Table 5.1 : List of proposed scintillators.

slot	scintillator	radiation sensor
1	4 different 70 mm×70 mm scintillators (FNAL)	K18, K21
2	15 finger scintillators in a row of 5 (FNAL)	K16, K39, K17
3	5 small finger scintillators (UMD)	K29, K22
4	EJ_200_P2 scintillator in Wetzel box (UMD)	K43
5	EJ_200_2X scintillator in Wetzel box (UMD)	no sensor
6	PEN scintillator in Wetzel box (UI)	K02, K20
7	PTP scintillator in Wetzel box (UI)	no sensor
8	PET scintillator in Wetzel box (UI)	K12, K13
9	QPAN scintillator in Wetel box (UI)	no sensor
10	SCSN81 scintillator in Wetzel box (UMD)	no sensor
11	EJ_260 scintillator in Wetzel box (UMD)	K41
12	Sensor plate	multiple sensors
13	AL4_2 scintillator in Wetzel box (UMD)	no sensor
14	AL4M_2 scintillator in Wetzel box (UMD)	no sensor

Centauro And Strange Object Research (CASTOR) table is receiving much radiation because it is in very forward region just after hadronic forward calorimeters between $5.2 < |\eta| < 6.6$ pseudo-rapidity region (Figure 5.1). Scintillators were prepared in a box for irradiation in CMS itself (Figure 5.2). Since luminosity and radiation level would be higher in HL-LHC phase, scintillators were put to CASTOR table which is close to beam pipe (Figure 5.3). This allowed to reach higher accumulated radiation doses to be able to observe radiation damage at HL-LHC luminosity. Irradiation were done by LHC 6.5 TeV energy beam in 2015. Integrated radiation level was expected to be around KRad by the end of 2015

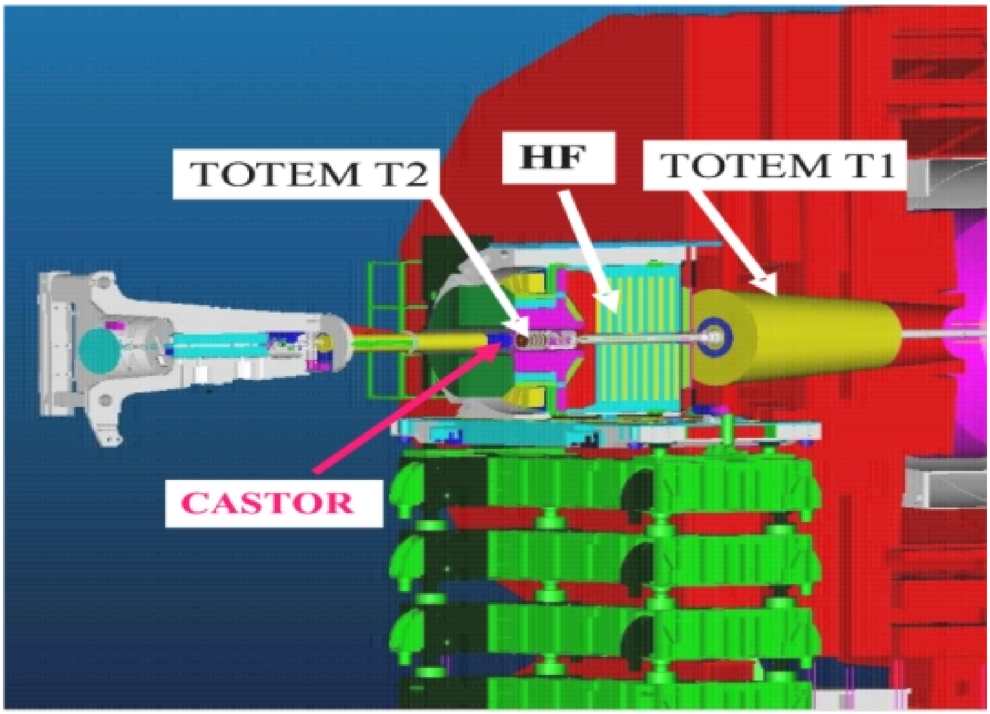

Figure 5.1 : CASTOR table location in CMS. Interaction point is in very right of the scheme. CASTOR is just after HF and it is in more forward region than HF calorimeters [27].

Figure 5.2 : Tiles in installation box. Slot numbers are increasing starting from the right side.

5.1.1 Measurement setup

Measurements of scintillators were done on the surface area at point 5 (CMS), not *in situ* on detector. Dubna scintillators were not measured since they have their own installation box and measurement setup. Only scintillators proposed by FNAL, UI and UMD were analyzed.

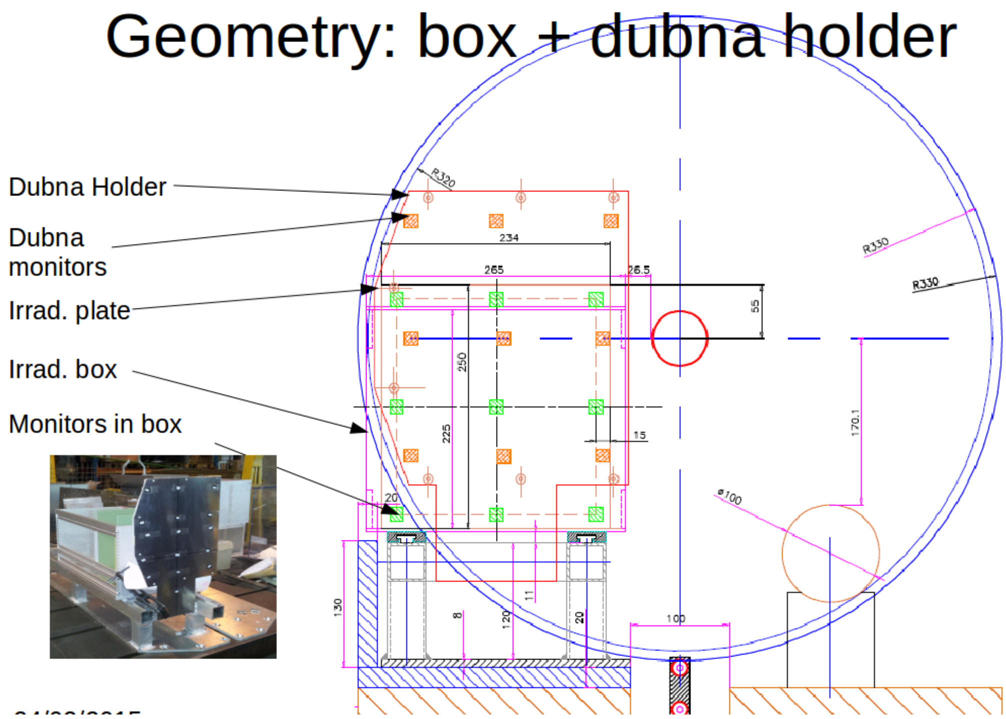

Figure 5.3 : Installation box (or irradiation box) in CASTOR table. Red circle is beam pipe. Box is 26.5 mm from the beam pipe. All dimensions are in mm.

Measurements were taken using SiPM, same detector as in the HE readout boxes. Since gain of SiPMs is sensitive to temperature and bias voltage, measurements were taken as current-volt $(I - V)$ curve where former is readout current from SiPM, latter is the bias voltage of SiPM. Measurement cycle is scintillator->fiber->SiPM->picoAM->GPIB_readout->local storage.

In this setup, scintillator, fiber, SiPM and beta source were in the dark box (Figure 5.4). Each scintillator was placed to a Wetzel box which is designed and 3D-printed by James Wetzel. There were two different aluminum plates to be placed on top of the Wetzel box, one with only one point for center of scintillator and one with four different points for corners of scintillators (Figure 5.5). These points were to put a beta source, Sr-90, as radioactive source. Data were taken by applying different bias voltage to SiPM and reading readout current by Keithley picoAmper meter. Keithley picoAmper meter supplied bias voltage to SiPM and read currents from SiPM. Keithley was controlled by local computer via general purpose interface bus (GPIB) readout module. Every command was sent by computer to Keithley via GPIB module.

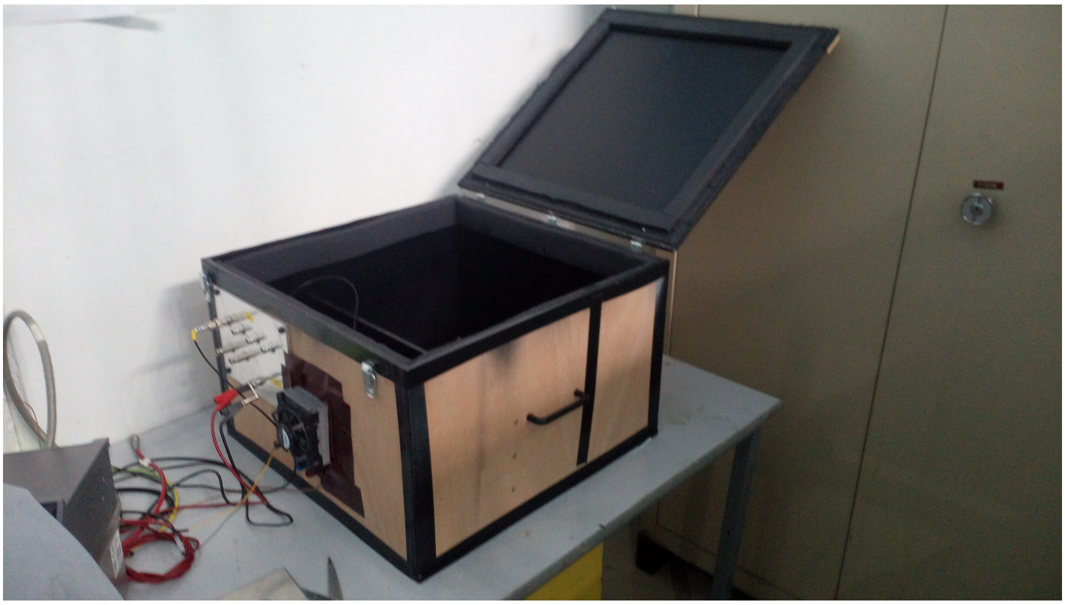

Figure 5.4 : Dark box where measurements are done on the surface of point 5.

Figure 5.5 : (a) Source position for measurements. Sr-90 beta source are placed at 5 different positions one by one as indicated in the figure. (b) Tiles are put into black 3D-printed Wetzel boxes during measurements.

In the installation box, there are 100 mm×100 mm scintillators between slot 4-11 inclusive and slot 13-14. There are small scintillators in the rest of the slots. For 100 mm×100 mm scintillators, 5 different source (1 at center and 4 at corners by aluminum plates) and 1 background measurement without source, were evaluated. For other scintillators, only 1 source measurement were taken while source was at the center, and 1 background measurement. After measurements, there are six measurements for 100 mm×100 mm scintillators and two measurements for the rest of the scintillators.

According to schedule, first measurements were taken in March 2015 with $85V-88V$ bias voltage range. Also repeatability measurements of the setup were taken in March. After first measurements, box of scintillators was placed on the CASTOR table for irradiation till next technical stop in June 2015. In June 2015, box of scintillators was brought to the surface from underground and same measurement procedure was applied. Scintillators, again, were lowered to CASTOR table until next technical stops in September and December 2015.

Measurements data are $I-V$ which have been taken by 50 mV steps in a certain range. Ten different measurements were taken for each voltage step. Each point in $I-V$ plots represents arithmetical means of 10 individual measurements for stability (Figure 5.6). These data were used for finding breakdown voltage (BDV).

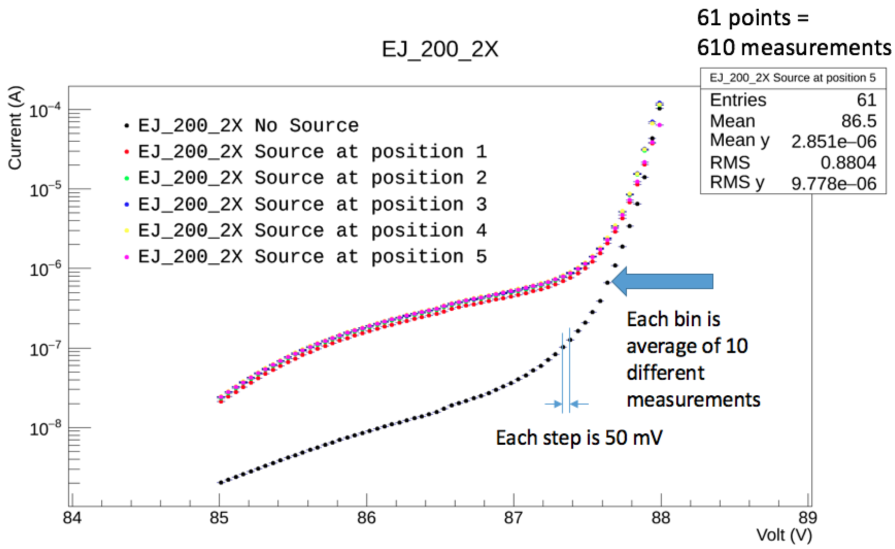

Figure 5.6 : An $I-V$ of a measurement of EJ_200_2X scintillator with 5 different source and a background measurements. Measurement step is 50vm$V$ and each point is the mean of 10 different measurements.

During measurements fibers were installed and uninstalled for several times to the scintillators, due to lack of fibers. Installing fiber to sigma-shape grooved scintillators caused some fibers to be scratched. And measurements had to be taken with scratched fibers. Scratched fibers would produce less light delivery, there would be less signal which will make almost impossible to compare 2 individual measurements.

Another important factor was temperature. SiPM are highly sensitive to temperature. It can sense 0.1 °C difference. For example, during June data taking, weather was to hot and there was a large difference in temperature during the day and the night and there was no air conditioner in the experimental room. This might have led to a change of BDVs even during the same measurement. In addition to these, there is no recorded info about temperature which might affect BDVs.

5.1.2 Analysis method

Once $I-V$ curves were taken from measurement of a scintillator, it is time to analyze the data. First of all, operating bias voltage range of SiPM needs to be determined. Gain of SiPM sensors is dependent on the temperature and bias voltage; moreover, the relation between gain and bias voltage is nonlinear. Relation between gain and temperature is around 8% per °C at 1.5 V above BDV [28]. In order to be able to compare 2 different measurements of the same scintillator, operating range must be matched.

Determining operating range of SiPM requires taking derivative of $I-V$ curve which is implemented by Yuri Musienko at CERN. This derivative then must be divided by corresponding current (I). This derivative was evaluated by numerical derivative method

$$\frac{\frac{dI}{dV}}{I} = \frac{\frac{I(V)-I(V+0.05)}{V-(V+0.05)}}{\frac{I(V)+I(V+0.05)}{2}} = 40 \times \frac{I(V)-I(V+0.05)}{I(V)+I(V+0.05)} \tag{5.1}$$

where I is SiPM signal current and V is bias voltage of SiPM. In this formulation, two neighboring points were used for calculating the derivative. After derivation, resulting plot will indicate 2 peaks on the plots. First peak will show breakdown voltage meaning the beginning of operating range. Second and bigger peak will indicate Geiger mode meaning the end of operating range (Figure 5.7). After Geiger mode, physics will change and one cannot distinguish leakage current and/or dark current. All comparison must be done between these two peaks. Operating range is around several volt. Applying Gaussian fit on the first peak, BDV can be easily extracted. BDV depends on temperature linearly. Since temperature could be different for all measurements for the same scintillator, BDV of all measurements must be found and matched. Then determining a ΔV and adding to the breakdown voltages, corresponding currents can be compared (Figure 5.8). Dividing currents at the corresponding voltages (at $BDV + \Delta V$), health status can be found. Subtracting that value from 1, radiation damage can easily be deducted.

$$Radiation\ Damage\ (RadDam) = 1 - \frac{I(BDV_{new}+\Delta V)}{I(BDV_{old}+\Delta V)} \tag{5.2}$$

These calculations were done for each measurements during the year of 2015 to be able to see radiation damage profile in time.

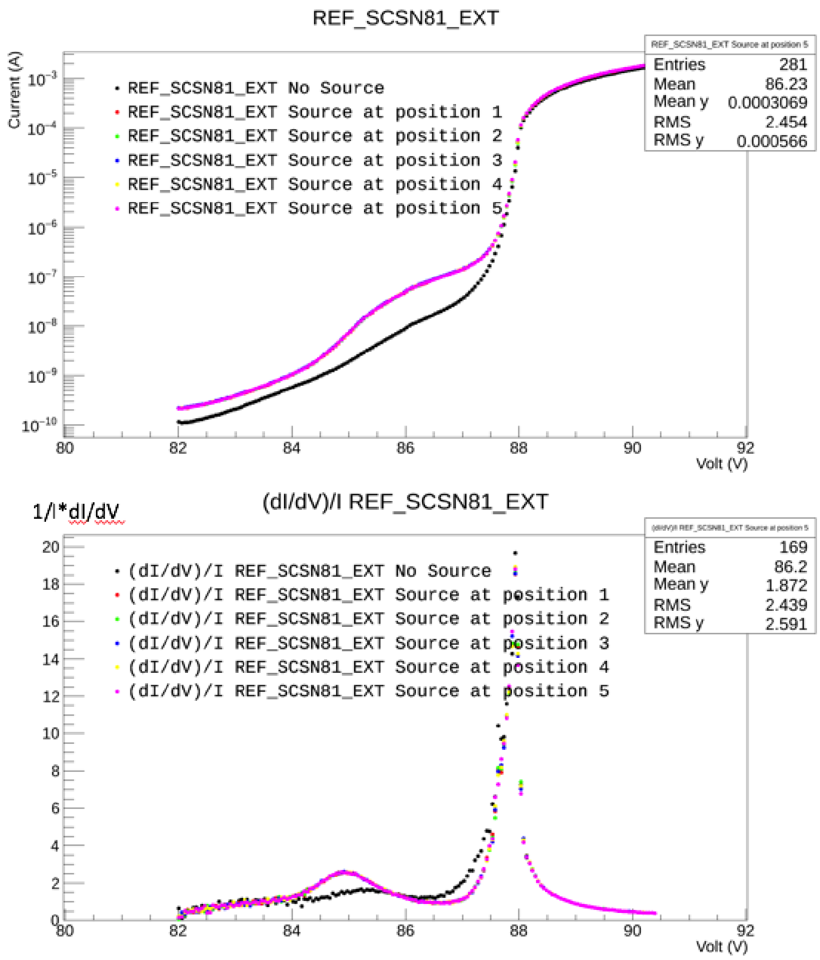

Figure 5.7 : Plot above shows 5 different source and a background $I-V$ curves. Plot below is the derivative of the first plot divided by current and it indicates breakdown voltage (first peak) and Geiger mode (second peak).

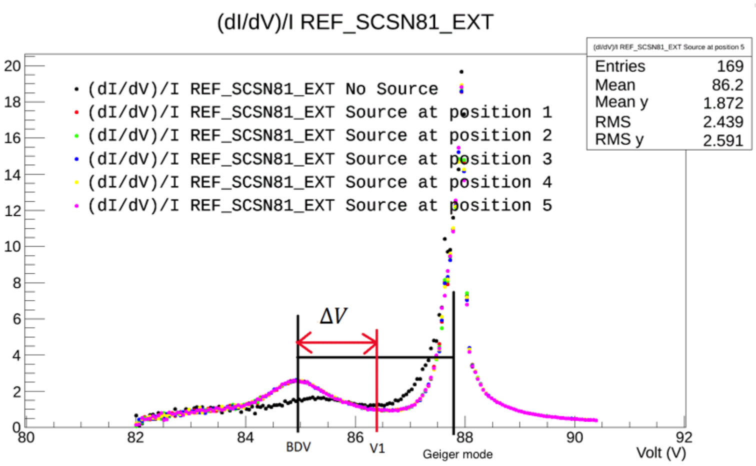

Figure 5.8 : Goal of measurements. First peak is breakdown voltage, second is Geiger mode. Comparison is done adding a ΔV to the breakdown voltage to compare in between these two peaks.

5.1.3 Repeatability of measurement setup

As in all scientific measurements, repeatability is important to determine systematic errors of measurement setup. For repeatability measurements, two of the scintillators were chosen, PEN (UI) and EJ_200_2X (UMD). Measurements were taken with full arrangement i.e. disconnecting, taking out of box, waiting around 20 minutes and connecting again. Six different measurements with source in the center were done for each of two of the scintillators in the range of $83V - 88V$ in March 2015. And also one background measurement was taken to subtract background noise for both scintillators.

First thing was to match BDVs using ROOT software package, since temperature was not controlled and not known. BDVs were almost the same with small differences; therefore, it was decided to correct for matching BDVs (Figure 5.9).

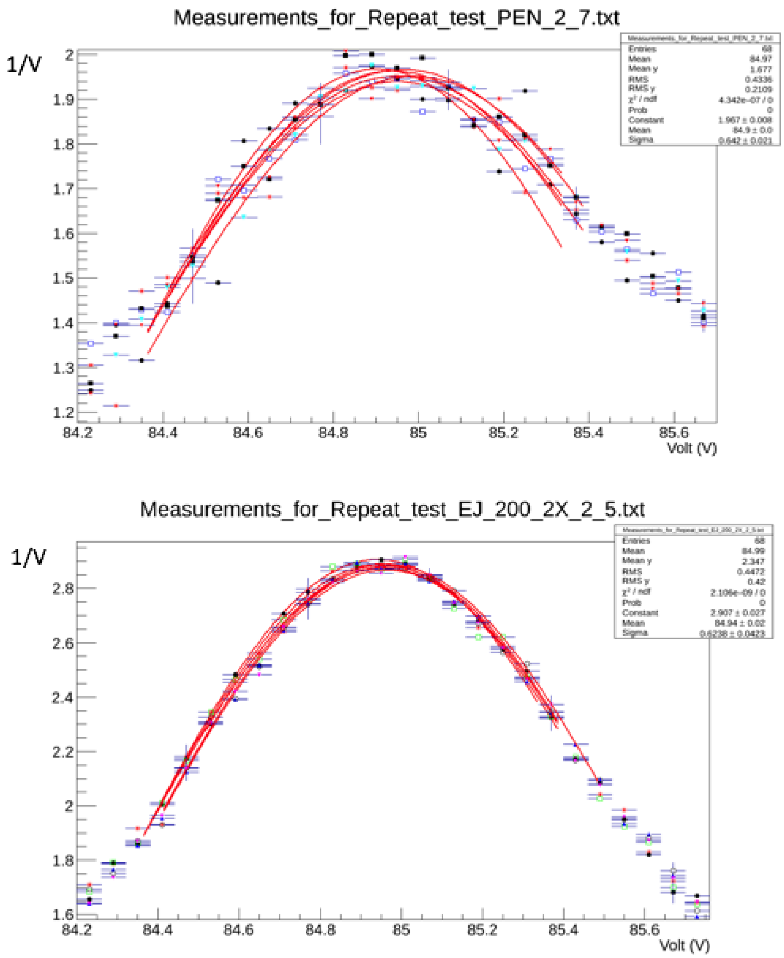

Figure 5.9 : Breakdown voltages of repeatability measurements. For all 6 measurements for both scintillator, breakdown voltages are almost same. Breakdown voltages were considered the same for repeatability analysis.

Two different methods were applied for repeatability. First one includes putting currents from each different measurements into individual voltage bin histograms. Histograms were filled for each voltage bin. Since there are six measurements, there were six entries for each histogram (Figure 5.10). Using means and root mean squares (RMS) of these histograms, systematic errors were determined for each bias voltage.

$$Systematic\ error = \frac{RMS(src\ measurements - background)}{Mean(src\ measurements - background)} \tag{5.3}$$

Repeating this process for each voltage, a profile histogram of systematic error can be obtained.

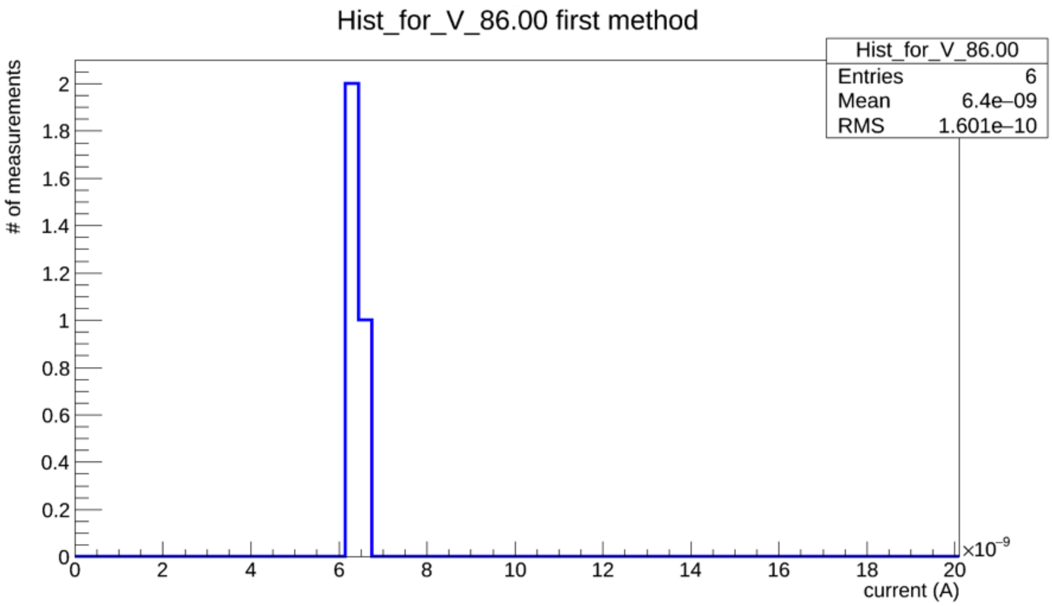

Figure 5.10 : Histogram for $V = 86V$ with first method. There are only six entries since there is only six measurements.

In the second method, if you recall that each point is the mean of 10 different measurements, better systematic error analysis can be done. Instead of putting six entries to each voltage histograms, 60 individual measurements can be put to the histograms (Figure 5.11). Again by evaluating equation 5.3 systematic errors are calculated.

5.1.4 Analysis of measurements

During 2015, four different measurements were taken in March, June, September and December. Results of these measurements must easily show radiation damage profile in time by comparing integrated luminosity during this period; therefore,

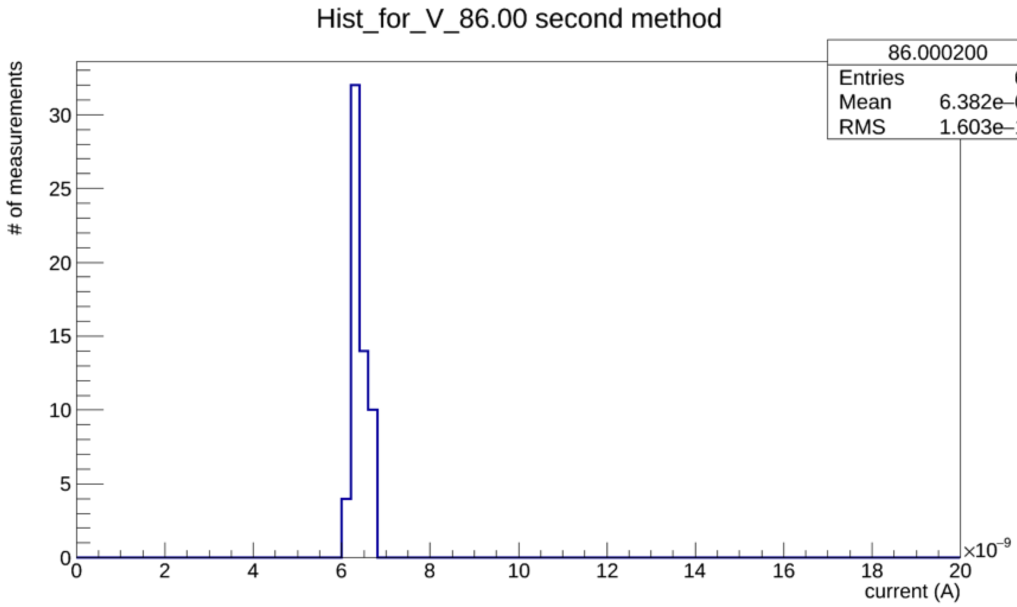

Figure 5.11 : Histogram for $V = 86V$ with second method. There are only 60 entries since there are 60 data taken in six measurements. Recall that each point in the measurement is the mean of 10 different measurements.

damage/radiation ratio can be calculated. When damage/radiation ratio is known, it can be estimated that how long scintillators will survive under integrated luminosity.

In March, voltage range for measurements does not include breakdown voltages. BDV of March measurements are around $85V$ and range is $85V - 88V$. Even if BDV of March measurements are slightly higher than $85V$, it is hard to determine BDV by Gaussian fit. For that reason, March measurements cannot be compared. However, in order to check consistency with next measurements, mean of BDVs from repeatability measurements in March $(84.96V)$ is used for breakdown voltage (Figure 5.9).

First measurements were in March 2015, but they cannot be used as reference measurements due to short voltage range, Luckily, there were no luminosity between March and June (Figure 5.12). This allows us to use June measurement as reference measurement before radiation. Starting from June, ranges were extended to include breakdown voltages.

In September and December, two different measurements were taken and analyzed with the same methods. Comparison was done by currents corresponding to $BDV + 0.6V$. Statistical error is around several percent. Current difference between two neighboring voltage bins (two bins with 50 mV difference) is around 10% in the range of $BDV + \Delta V$. If $BDV + \Delta V$ is in between two neighboring voltage bins, choosing

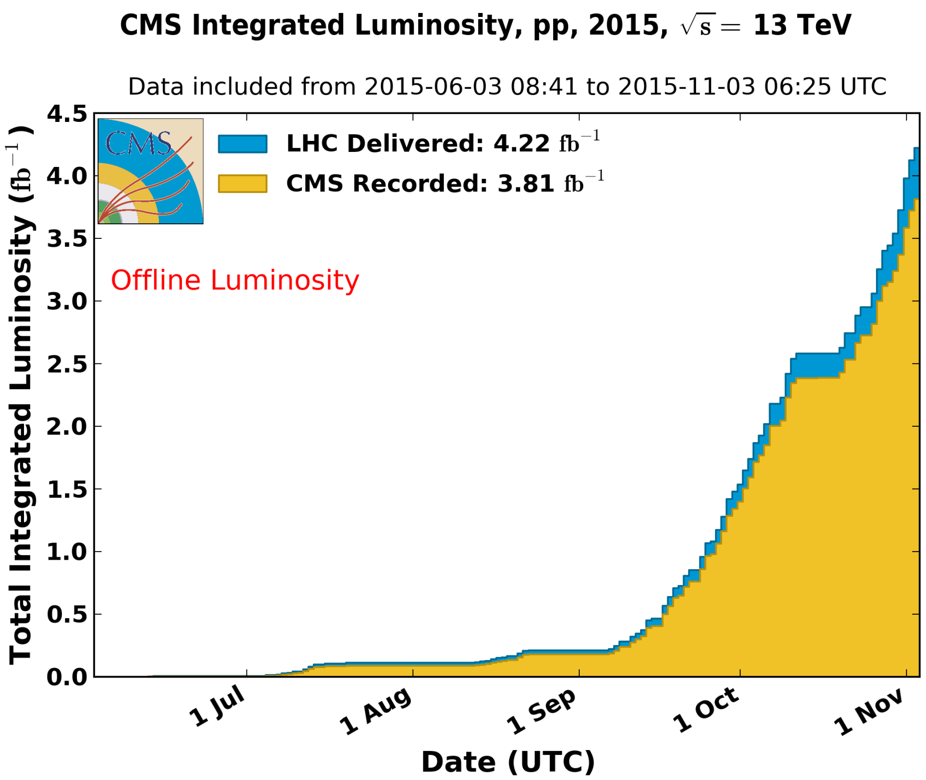

Figure 5.12 : CMS integrated luminosity between June 2015 and November 2015. Before June 2015 there is no beam [29].

the closest voltage will add a statistical error of around 5%. However, this error was reduced by using spline cubic interpolation. Instead of choosing the closest neighbor voltage, interpolation value was used for $BDV+\Delta V$. Statistical error was reduced to a reasonable level.

5.2 Hadronic Forward Calorimeters 2014 and 2016 Sourcing Analysis

Due to upgrade requirements, PMTs of forward calorimeters (Hamamatsu R7525) have been replaced with new ones (Hamamatsu R7600) in LS1. In Run 2, gains of new PMTs become important to determine the energy deposited in HF channels. For that reason, local sourcing measurements were done with Co-60 radioactive source. First sourcing runs were taken in April 2014 for HF plus (HFP) and in July 2014 for HF minus (HFM) after installation of PMTs. Sourcing was done by source driver which consists of Co-60. This source driver has a Co-60 source in one end and can penetrate inside the HF tubes. Source driver is driven by the run control and monitor system (RCMS) automatically. It can also indicate position of the source inside tube. This position info is correlated with the data to produce a profile through the fiber.

The source was run through the end of each HF channels one by one, but data are taken from all channels. Since lengths of fibers are not the same for all channels and some part of fibers are outside of absorber, data must be analyzed starting from point where source inside the absorber for each channel. Lengths of fibers are different outside of channels; therefore, starting indices are different for each channel. In each channel there are two different tubes, one for electromagnetic and one for hadronic part. Electromagnetic tubes are 1.65 m and longer than hadronic tubes. Hadronic fibers are 1.43 m inside the absorber (Figure 5.13). When signal is profiled versus real position in mm there will be a big peak just before starting point and then there will be a straight line around 1.65 m which is the length of the fiber inside the absorber (Figure 5.14). For hadronic fibers there will be a drop in signal around the last 22 cm, since there is no fiber after 1.43 m. Events were taken into analysis when source position is between

$$Tube\ Start + 300\ mm < Source\ Reel\ Position < Tube\ End - 300\ mm \tag{5.4}$$

Tube start position and tube end position are different for each tube depending on fiber length outside of the absorber. Each wedge covers 20° degree in ϕ and $29 < i\eta < 41$ in $i\eta$ space (Figure 5.15).

Charge is collected by 4 capacitors for each 25 ns –1 time slice (TS)– and 50 ns –2 TS. Signal from four different capacitors must be summed over. Integrated charge is registered via analog to digital converter (ADC). For different TS firmware, bin weights ADC are different. For 1 TS charges; 15 bins weighted by 1, 7 bins weighted by 2, 4 bins weighted by 3, 3 bins weighted by 4 and 3 bins weighted by 5, and in total range is between 0-63 ADC counts. 32nd and the last bin is overflow containing all charges above 64. For 2 TS charges; 10 bins weighted by 1, 6 bins weighted by 2, 5 bins weighted by 4, 5 bins weighted by 8, 3 bins weighted by 16, 2 bins weighted by 32 and 1 bin weighted by 62, and range is between 0-194 ADC count. 32nd and the last bin contains charges above 194.

Analysis were done by CMS software package (CMSSW_5_3_11_patch5). In the first bins for 1 TS data, there will be a peak of ADC counts in log scale plots (Figure 5.16).

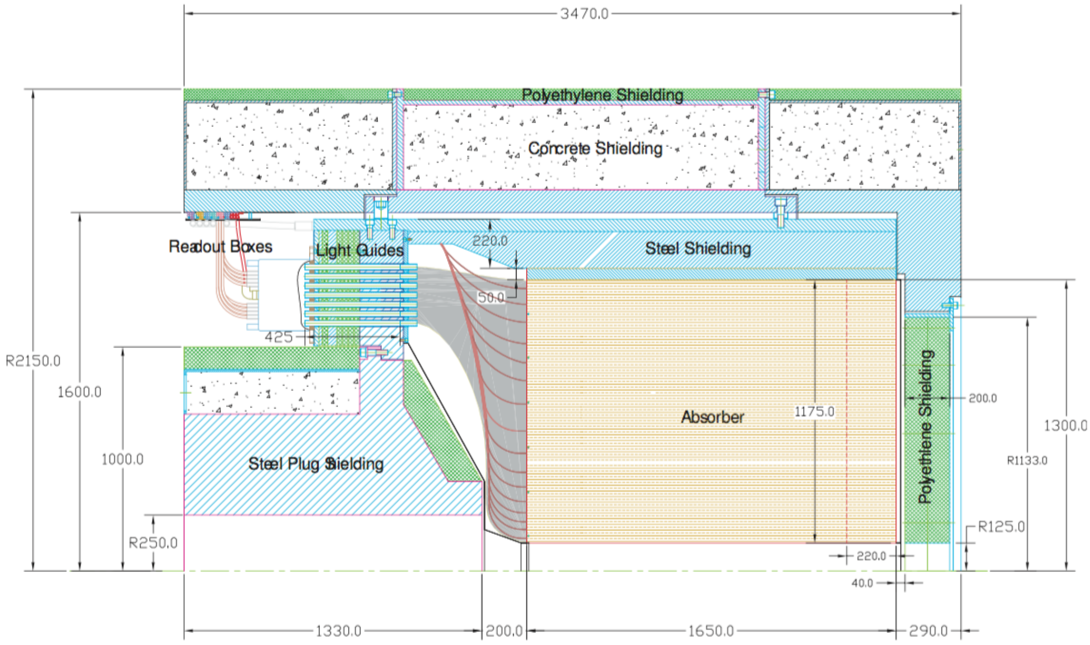

Figure 5.13 : The cross section view of the HF calorimeter shows that the sensitive area extends from 125 to 1,300 mm in the radial direction. The absorber in the beam direction measures 1,650 mm. Bundled fibers (shaded area) are routed from the back of the calorimeter to air-core light guides which penetrate through a steel-lead-polyethlene shielding matrix. Light is detected by PMTs housed in the readout boxes. Stainless steel radioactive source tubes (red lines) are installed for each tower and are accessible from outside the detector for source calibration. The intersection point is at 11.15 m from the front of the calorimeter to the right. All dimensions are in mm [30].

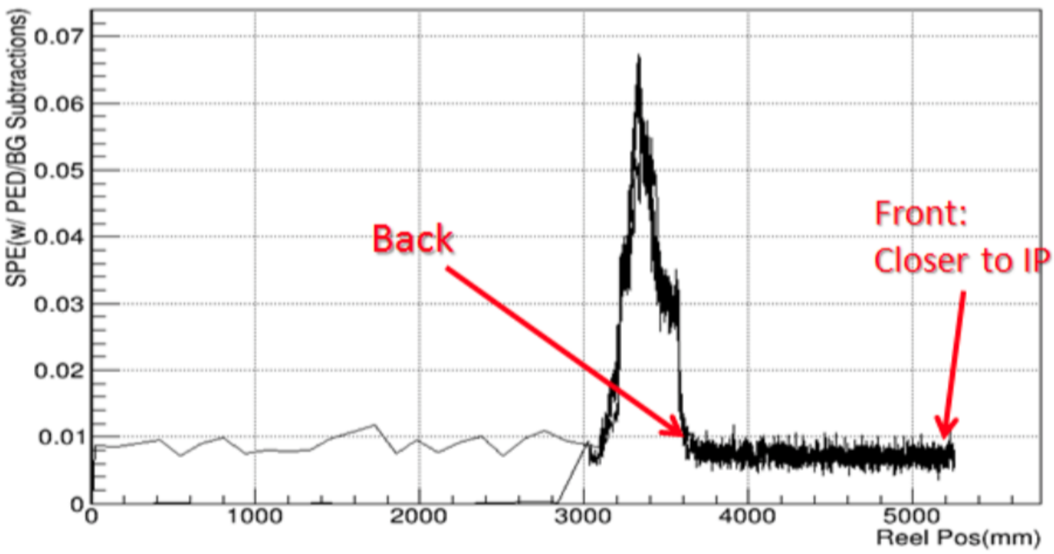

Figure 5.14 : HF sourcing data profile. For this individual channel tube starts around 3,600 mm and continue around 5,200 mm [31].

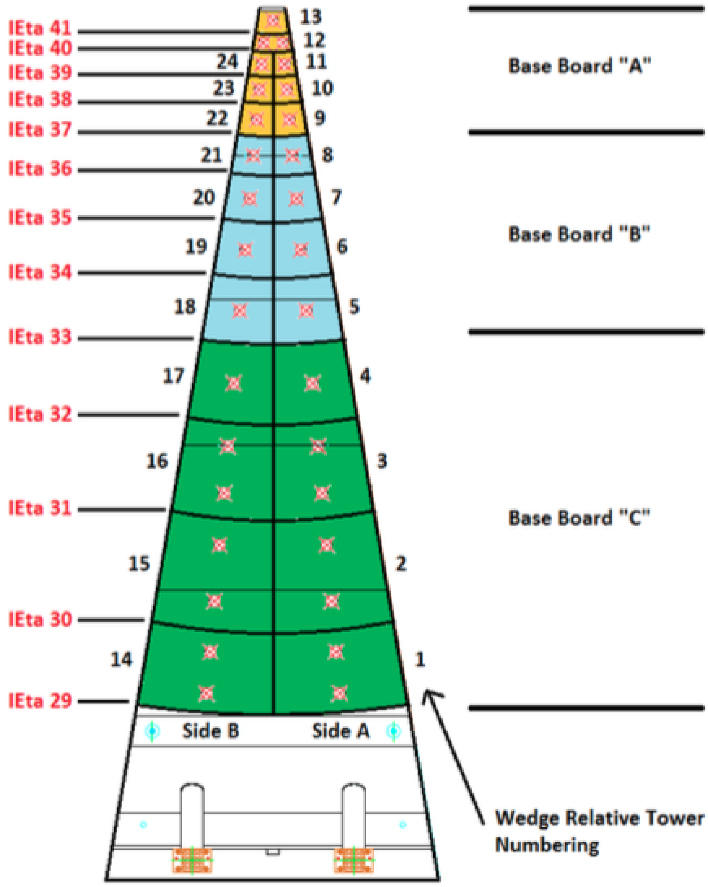

Figure 5.15 : Schematics of an HF towers. Beam pipe is close to the upside; therefore, $i\eta$ numbers are getting bigger going up. Each channel is connected to three baseboards which includes eight PMTs in each [31].

This shows the pedestal region peak due to capacitor delay, and Gaussian mean of this peak must be subtracted in calculations.

Signal from one channel is called source signal, if source is in the same channel. Signal from one channel is called background signal if source is in same wedge but far from the channel. Taking the difference of source and background signals, charge can be calculated for the individual channels. Source and background signals can be calculated by

$$Q_{signal} = \frac{\sum_{i=1}(q_s - q_s^{ped})n}{\sum_{i=1}^{32} n} = \frac{\sum_{i=1} q_s n}{\sum_{i=1}^{32} n} - q_s^{ped} \tag{5.5}$$

$$Q_{background} = \frac{\sum_{i=1}(q_b - q_b^{ped})n}{\sum_{i=1}^{32} n} = \frac{\sum_{i=1} q_b n}{\sum_{i=1}^{32} n} - q_b^{ped} \tag{5.6}$$

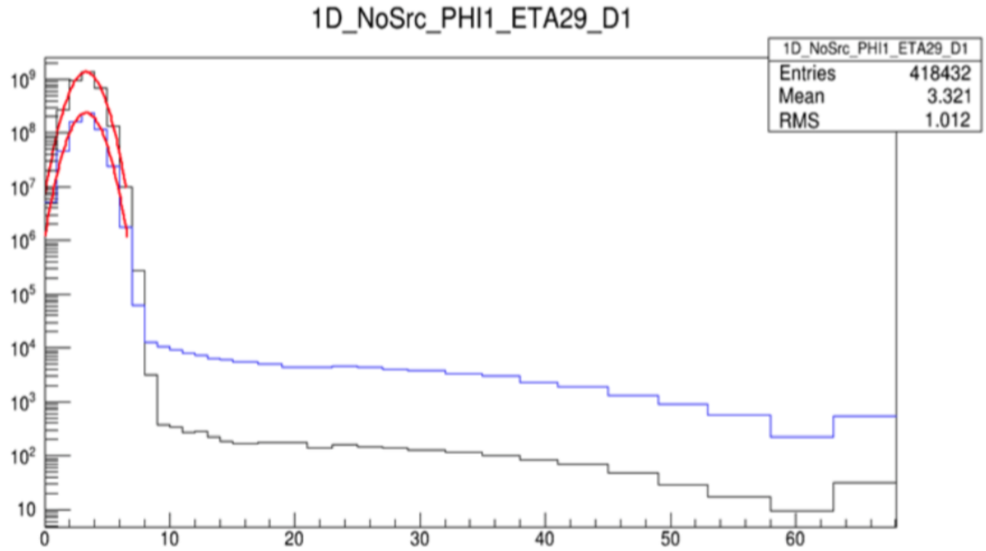

Figure 5.16 : HF sourcing data histogram for each event. Peak in left is due to capacitors and mean of this peak needs to be subtracted from accumulating signal for all events [31].

$$Q_{signal}^{uncorrected} = Q_{signal} - Q_{background} \tag{5.7}$$

where q^{ped} is Gaussian mean of pedestal region, n is the charge of i^{th} bin (y-axis in Figure 5.16), q is the ADC counts (x-axis in Figure 5.16).

Background parameters are:

While source is in $i\eta = 29$, background was recorded in towers $i\eta \geq 34$,

While source is in $i\eta = 39$, background was recorded in towers $i\eta < 34$,

Once source signal and background signal constructed by subtracting pedestals for each channel, next thing to do is geometrical corrections. Cell dimensions are not the same for all channels; thus, energy deposition on cells will not be the same for each tube. Geometric correction factors determined by Geant4 simulation was applied to the signals by

$$Q_{signal}^{corrected} = Q_{signal}^{uncorrected}/R \tag{5.8}$$

where R is the geometric correction factor in Table 5.2.

Table 5.2 : Geometric correction factors for each tower's energy containment for a radioactive source passing through a given source tube [31].

Tube	Mismatch	Match	Unc.
1(14)A	0.917	0.840	0.017
1(14)B	0.909	0.833	0.017
2(15)A	0.945	0.866	0.009
2(15)B	0.938	0.859	0.009
3(16)A	0.925	0.846	0.013
3(16)B	0.908	0.829	0.015
4(17)	0.930	0.851	0.002
5(18)	0.889	0.810	0.003
6(19)	0.847	0.772	0.004
7(20)	0.789	0.713	0.006
8(21)	0.715	0.633	0.018
9(22)	0.646	0.572	0.006
10(23)	0.597	0.516	0.013
11(24)	0.498	0.425	0.023
12A(B)	0.413	0.331	0.056
13	0.588	0.510	0.023

Next correction would be ADC count to fC conversion. According to Hamamatsu handbook, ADC/fC conversion coefficient is 2.6. Multiplying results by 2.6, average charges for each channel were calculated in fC unit.

Groove types of HF tubes are different, either hadronic or electromagnetic. If source tube replaced an electromagnetic optical fiber, fC/GeV conversion coefficient is 744.6 KeV. If source tube replaced a hadronic optical fiber, fC/GeV conversion coefficient is 706 KeV. Multiplying charges with corresponding numbers according to groove type map, ADC/GeV conversion were calculated. These coefficients are calibration coefficients of HF PMTs and sent to the conditions database (CondDB) for Run 2 collisions. New HF sourcing data has been taken in 2016 and these data will be analyzed in 2016. Due to changes in HF electronics in LS1, CMSSW_5_3_11_patch11 cannot unpack HF data; hence, analyzer code was upgraded to newer version of CMSSW (above CMSSW_7_3_5_patch6) which includes HF new electronics map. Also analyzer code requires a new upgrade due to new charge integrated encoder (QIE) card. Installed QIE cards are QIE8. In few channel of HF, there are QIE10 cards. All QIE cards of HF will be replaced by QIE10 cards. New analyzer needs to unpack QIE10 data as well.

5.3 Radiation Damage Monitoring of Hadronic Forward Calorimeter Fibers

HCAL is exposed to radiation from collisions. In forward regions where HF calorimeters sit, radiation level is comparatively much higher than the rest of the detector. HF fibers will be damaged while integrated luminosity is increasing. An optical reflectometry system developed and installed to some HF channels to monitor radiation damage and fiber recovery. Rapid optical transparency assessment is required due to dynamic nature of damage and recovery. This rapid assessment becomes more important around wavelength region where PMTs are the most sensitive.

Monitoring of fibers requires to use 337 nm pulsed nitrogen laser. However wavelength of laser is shifted by a 2 cm long scintillating fiber into blue region ($\sim$ 440 nm). Shifted laser light is distributed to 56 HF channels in four wedges. These 56 HF channels will provide radiation damage profile of the entire system. Some fraction of laser light reflects from an optical connector which is installed to radiation damage channels. Rest of the laser light will take the whole path through fibers and turn back. On PMT readout plot there will be two signals; first one due to direct reflection reflection of laser, second one is from reflection the end of the fiber where traveling the whole fiber back and forth. Optical connectors are placed on the HF fiber so that time window becomes 25 ns (1 TS) (Figure 5.17). Ratio of these signals should remain the same for each channel if there is no radiation damage. Ratio for individual channels might differ from each other; however, ratios will decrease in time depending on the radiation damage. Fibers will deliver less number of photons which will result as a decrease in ratio profile in time.

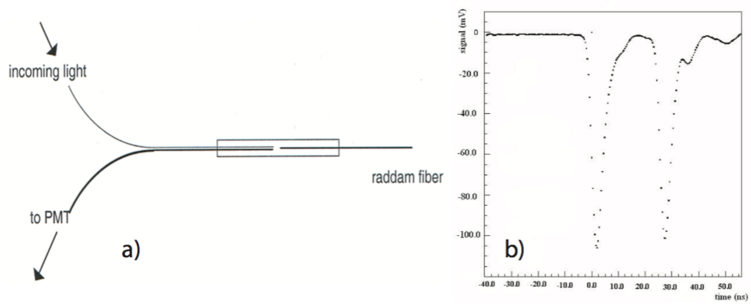

Figure 5.17 : The radiation damage to the optical transparency is monitored by a set of 56 fibers distributed in the entire calorimeter system. The ratio of the reflected pulse from the far end of the fiber located inside the absorber to the reflected pulse from the first optical connector provides a relative measure of fiber darkening. A schematic of optical connection is depicted in (a) and a pulse train is reproduced in (b). [30]

HF radiation damage data are taken time to time in years. In each data there will be pulse shape distribution along 10 TS. Reflected and transmitted signal will appear in two consecutive time slices as S1 and S2, since delay between these two signals is 25 ns (Figure 5.18).

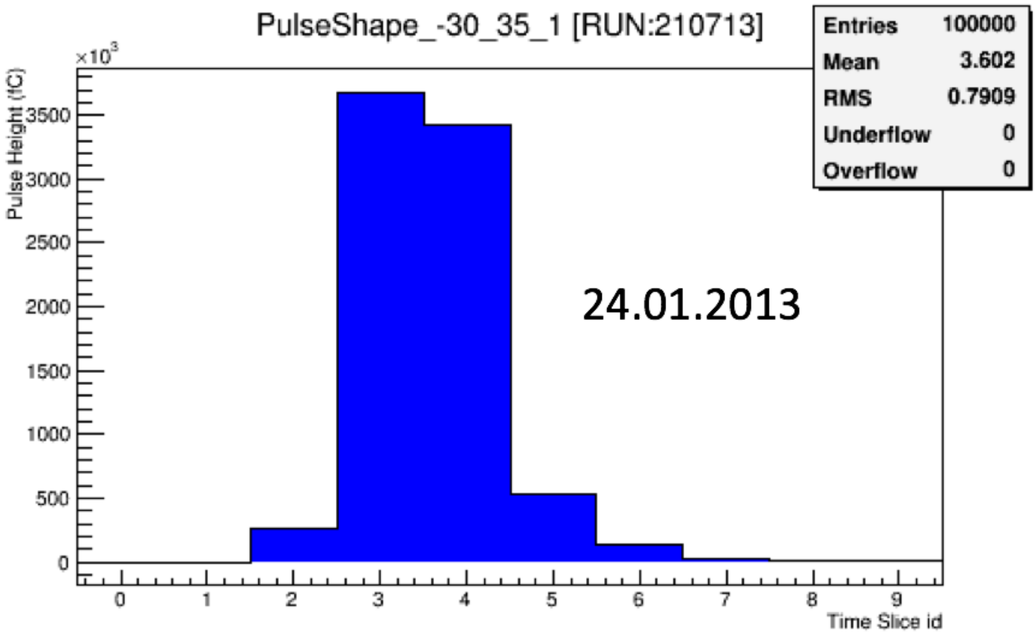

Figure 5.18 : Pulse shape of an HF radiation damage channel. $X-$axis is time slice. Each time slice is 25 ns width. There are 2 signal peaks which corresponds to reflected and transmitted signal from optical connector, respectively. Transmitted signal height will be related to fiber health.

Generating these pulse shapes and calculating ratios by CMSSW software, radiation damage profile of HF fibers can be monitored. One of the data will be chosen as reference, then all data taken after reference data will be divided by results of reference data. Hence, first ratios will be 1 for each radiation damage channel. Then it is expected that this ratio will decrease in time.

5.4 Online Software Development

In context of online software development, new generation readoutboxes manager (ngRBXManager) requires upgrade.

This manager handles collection of data from readout boxes and provides a user interface. Sending command and having response from new generation clock control module (ngCCM), it can control a whole crate. As of April 2016, there are problems about communication with ngCCMs. First of all commands must be delivered successfully to ngCCM and then feedback must be received about the command delivery status. After fixing this problem, new features will be proposed and developed. Studies are still continuing with this issue.

6. RESULTS AND CONCLUSIONS

6.1 Hadronic Endcap Calorimeter Scintillator Upgrade

After 4 different measurement periods in March, June, September and December in 2014, it can be easily seen that there is a problem about reliability of measurement setup. Some measurements are negative or bigger than 1 which should be impossible (Table 6.1).

Table 6.1 : Results of measurements.

scintillator	Jun (A)	Sep (A)	Dec (A)	Sep/Jun	Dec/Jun
EJ_200_2X	8.29×10^{-8}	6.43×10^{-8}	3.35×10^{-8}	0.776	0.404
EJ_200_P2	6.33×10^{-8}	6.74×10^{-8}	2.01×10^{-8}	1.065	0.318
EJ_260	1.28×10^{-8}	1.20×10^{-8}	6.54×10^{-9}	0.940	0.512
PEN	1.44×10^{-9}	1.94×10^{-9}	6.48×10^{-10}	1.350	0.450
PET	2.83×10^{-10}	-1.11×10^{-9}	1.07×10^{-10}	−3.941	0.379
SCSN81	1.48×10^{-8}	1.52×10^{-8}	9.85×10^{-9}	1.032	0.667
FNAL_93	2.73×10^{-8}	2.21×10^{-8}	1.68×10^{-8}	0.809	0.614
FNAL_94	3.72×10^{-8}	2.79×10^{-8}	2.12×10^{-8}	0.749	0.568
FNAL_95	4.13×10^{-8}	4.57×10^{-8}	2.23×10^{-8}	1.106	0.539
FNAL_96	2.79×10^{-8}	8.52×10^{-9}	4.15×10^{-9}	0.305	0.149

From March repeatability measurements, profile histograms for two different methods for both measured scintillators clearly indicate that there are systematic errors around 5% for EJ_200_2X scintillator (UMD) and 3% for PEN scintillator (UI) (Figure 6.1). This by itself is enough to consider this measurement setup as unreliable, since expected radiation damage level should be around several percent in 2015 LHC luminosity.

Under these circumstances and meaningless results, experiment will be redone *in situ* on CASTOR table. Instead of using Keithley picoAM and GPIB readout system, data will be taken by HCAL RCMS. As of April 2016, new boxes have been shipped to CERN from FNAL. New readout modules (RM) are now being calibrated. New FE and BE electronics are also being setup. Plan is to install everything with electronics to

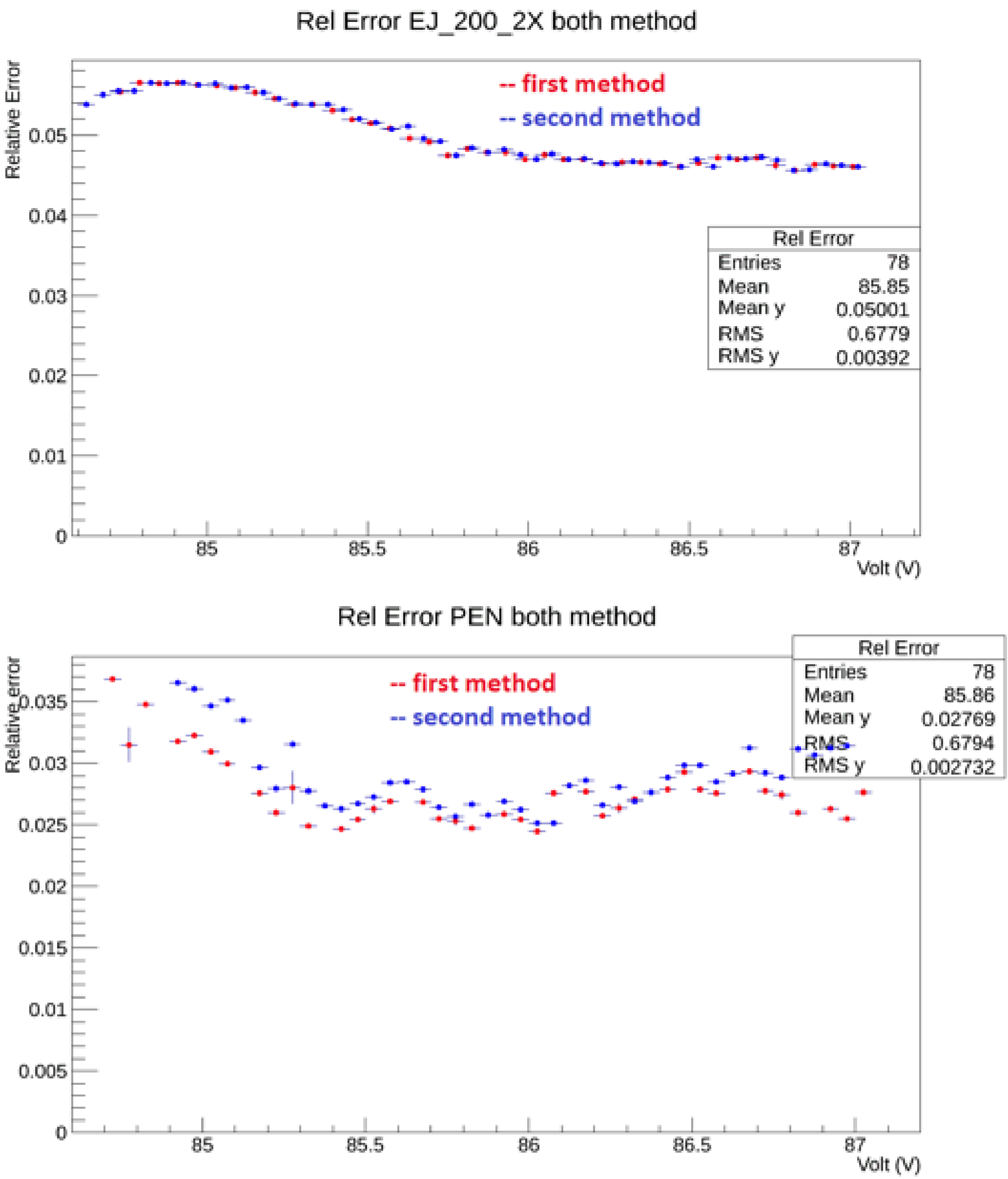

Figure 6.1 : Results of repeatability measurements.

the CASTOR table in June 2016 technical stop. Measurements will be taken by HCAL DAQ system hoping to have reliable results.

In building 28 at CERN, calibration studies of RMs still continue. Mapping of scintillator boxes are being done by LED and laser data taken by RCMS. After completion of mapping and calibration works, all teststands will be transferred to point 5 to be installed to underground service cavern (USC) of the CMS. Same tests will be repeated to integrate RMs and installation box to the HCAL DAQ system. After installing box to the CASTOR table, new measurements can start for more reliable results. In 2016 new measurements will clearly indicate the radiation damage, and radiation damage level will be one of the most important criteria for HE scintillators selection.

6.2 Hadronic Forward Calorimeters 2014 and 2016 Sourcing Analysis

HF 2014 sourcing analysis has been finished as of December 2014 and new gains are being used for calibration coefficients of the HF PMTs. Calibration coefficient show a narrow distributions (Figure 6.2). In the results there are no unexpected problems.

In January 2016 new HF sourcing data were taken, same procedure will be applied for new data and gains of PMTs will be recalculated. This will be a great chance to check consistency of two sourcing measurements

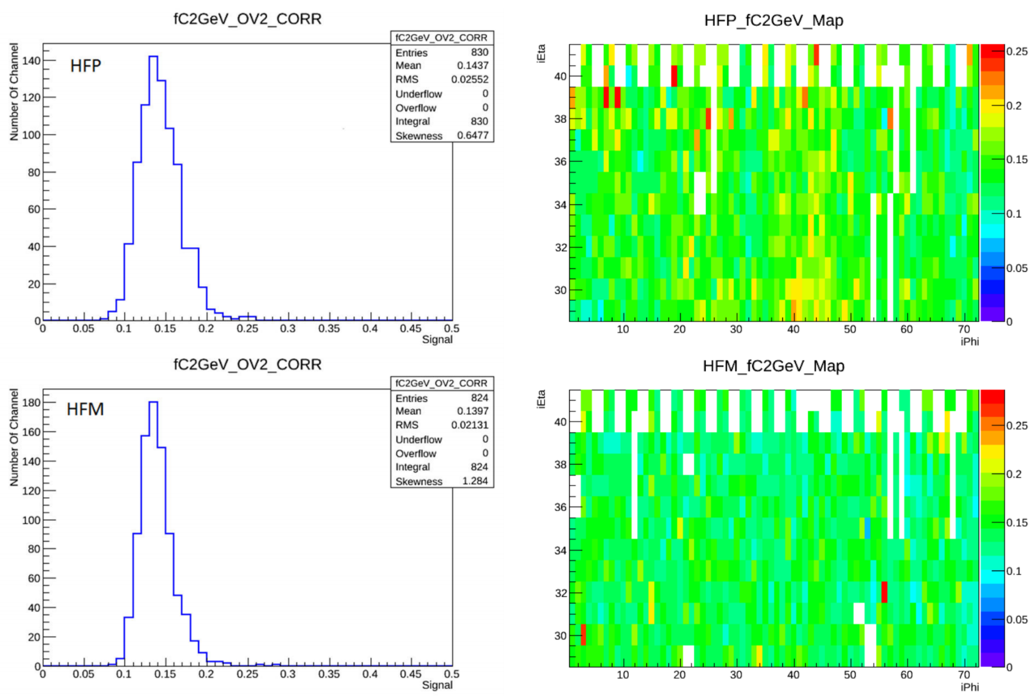

Figure 6.2 : Results of HF sourcing calibration measurements. Left plots are distribution of calibration coefficients. Right plots are map of calibration coefficients of HF PMTs.

6.3 Radiation Damage Monitoring of Hadronic Forward Calorimeter Fibers and Online Software Development

HF calorimeter fiber damage studies are done for Run 1 (Figure 6.3). It clearly shows that fiber health is decreasing as expected. These monitoring requires long term work on HF radiation damage issue. As long as HF operates, there will be increasing radiation.

Online software upgrades for ngRBXManager is another ongoing work. Before going further, it needs to be decided what it should do. After this decision and fixing the communication problem, time will come to proceed with new features.

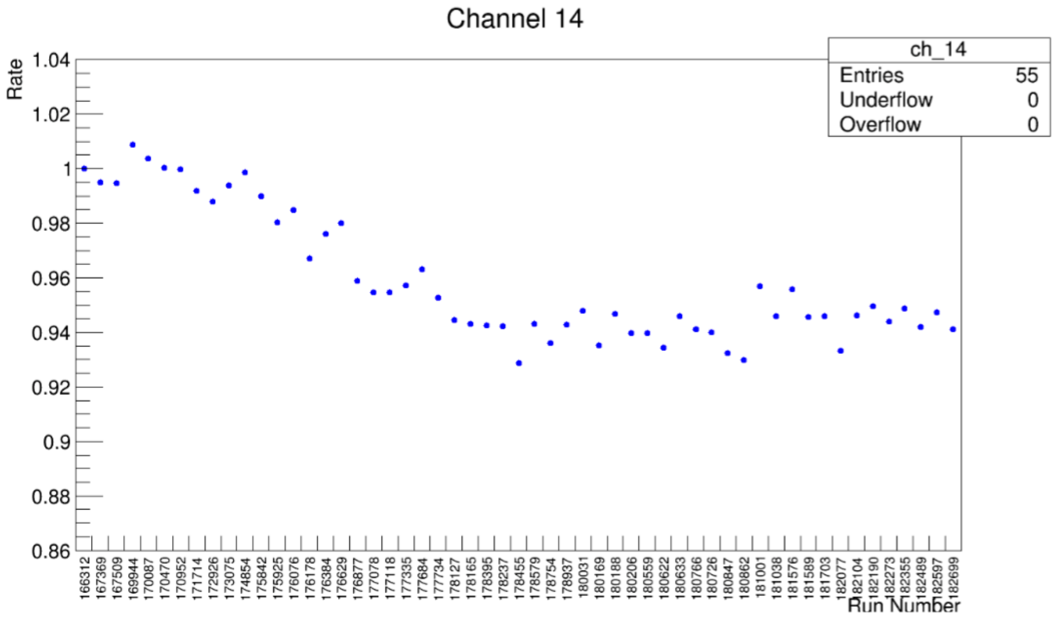

Figure 6.3 : An example for radiation damage profile of HF fibers. First data point is the reference and all other data points are divided by this reference data revealing a clear indication of damage.

REFERENCES

[1] **Dalton, J.** (1808). *A New System of Chemical Philosophy Part 1*, London and Manchester: S. Russell.

[2] **Thomson, J.J.** (1893). Cathode Rays, *Philosophical Magazine*, *44*, 293.

[3] **Rutherford, E.** (1919). Collision of α Particles with Light Atoms IV. An Anomalous Effect in Nitrogen, *Philosophical Magazine*, *37*, 581.

[4] **Dirac, P.A.M.** (1928). The Quantum Theory of the Electron, *Proc. R. Soc. Lond*, *117*, 610–624.

[5] **Anderson, D.C.** (1932). The Apparent Existence of Easilly Deflectable Positives, *Science*, *76*(1967), 239–248.

[6] **Neddermeyer, S.H. and Anderson, D.C.** (1937). Note on the Nature of Cosmic-Ray Particles, *Physical Review*, *51*(10), 884–886.

[7] **Rochester, G.D. and Butler, C.C.** (1947). Evidence for the Existence of New Unstable Elementary Particles, *Nature*, *160*(4077), 855–857.

[8] **Chamberlain, O.**, **Segre, E.**, **Wiegand, C. and Ypsilantis, T.** (1955). Observations of Antiprotons, *Physical Review*, *100*(3), 947–950.

[9] **Cowan, C.L. and Reines, F.** (1956). The Neutrino, *Nature*, *178*, 446–449.

[10] **Danby, G.** *et al.* (1962). Observation of High-Energy Neutrino Reactions and Existence of Two Kinds of Neutrinos, *Physical Review Letters*, *9*(1), 36–44.

[11] **Bloom, E.D.** *et al.* (1969). High Energy Inelastic e-p Scattering 6° and 10°, *Physical Review Letters*, *23*(16), 930–934.

[12] **Aubert, J.J.** *et al.* (1974). Experimental Observation of a Heavy Particle J, *Physical Review Letters*, *33*(23), 1404–1406.

[13] **Augustin, J.E.** *et al.* (1974). Discovery of a Narrow Resonance in e^+e^- Annihilation, *Physical Review Letters*, *33*(23), 1404–1406.

[14] **Herb, S.W.** *et al.* (1977). Observation of a Dimuon Resonance at 9.5 GeV in 400-GeV Proton-Nucleus Collisions, *Physical Review Letters*, *39*(5), 252–255.

[15] **Abe, F.** *et al.* (1995). Observation of Top Quark Production $\bar{p}$p Collisions with the Collider Detector at Fermilab, *Physical Review Letters*, *74*(14), 2626–2631.

[16] **Arabuchi, S.** *et al.* (1995). Observation of the Top Quark, *Physical Review Letters*, *74*(14), 2632–2637.

[17] **Barber, D.P.** *et al.* (1979). Discovery of Three-Jet Events and a Quantum Chromodynamics at PETRA, *Physical Review Letters*, *43*(12), 830–833.

[18] **Aubert, J.J.** *et al.* (1983). The Ratio of The Nuclean Structure Functions F_2^N for Iron and Deuterium, *Physical Letters B*, *123*(3-4), 275–278.

[19] **Arnison, G.** *et al.* (1983). Experimental Observation of Lepton Pairs of Invariant Mass Around 95 GeV/c^2 at the CERN SPS Collider, *Physical Letters B*, *126*(5), 398–410.

[20] `http://press.web.cern.ch/press-releases/2012/07/cern-experiments-observe-particle-consistent-long-sought-higgs-b` date: July 4, 2012.

[21] `http://home.web.cern.ch/about/updates/2013/03/new-results-indicate-new-particle-higgs-boson`, date: March 14, 2013.

[22] **Bais, S.**, (2005). The Equations:Icons of Knowledge.

[23] **CMS** (1997). The Hadron Calorimeter Technical Design Report, **Technical Report 1997-031**, CERN/LHCC, cMS TDR 2.

[24] **CMS** (2006). CMS Physics Technical Design Report, Volume 1 Detector Performance and Software, **Technical Report 2006-001**, CERN/LHCC, cMS TDR 8.1.

[25] `http://hilumilhc.web.cern.ch/about/hl-lhc-project`, date: February 22, 2016.

[26] **CMS** (2010). Technical Proposal for the Upgrade of the CMS detector Through 2020, **Technical Report 2010-004**, CERN/LHCC.

[27] `http://cmsdoc.cern.ch/cms/castor/html/`, date: April 30, 2016.

[28] **Anderson, J.** *et al.* (2012). CMS Colloboration, *Phys. Procedia*, volume 37, pp.72–78.

[29] `https://twiki.cern.ch/twiki/bin/view/CMSPublic/LumiPublicResults#2015_Proton_Proton_13_TeV_Collis`, date: April 18, 2016.

[30] **Cankoçak, K.** *et al.* (2006). Design, Performance, and Calibration of CMS Forward Calorimeter Wedges, **CMS Note 2006-044**, CERN-CMS.

[31] **Atay, S.** *et al.* (2015). Calibration of the CMS Hadron Forward Calorimeter in preparation for Run II, **CMS Note 2015-006**, CERN-CMS, draft.

CURRICULUM VITAE

Name Surname: Serhat Atay

Place and Date of Birth: Tavas, 25/11/1989

Adress:

E-Mail: serhat.atay@cern.ch

B.Sc.: Physics Engineering / Mathematics Engineering

M.Sc.: Physics Engineering

Professional Experience and Rewards: Researcher at CERN

List of Publications and Patents:

Atay, S. et al. (2012). Introduction and Concept Design of the "AUVTECH" Istanbul Technical University Autonomous Underwater Vehicle, AUVSI & ONR's 15th RoboSub Competition Journal Paper.

Atay, S. et al. (2015). Calibration of the CMS Hadron Forward Calorimeter in preparation for Run II, CMS Note 2015-006, CERN-CMS, draft.